Accurate Parameter Estimation on Photovoltaic Modules Using Fisher Information Matrix and D-Optimal Design

IEEE Access
Multidisciplinary | Rapid Review | Open Access Journal

Received 7 October 2025, accepted 4 December 2025, date of publication 15 December 2025,
date of current version 19 December 2025.

Digital Object Identifier 10.1109/ACCESS.2025.3643942

RESEARCH ARTICLE

Accurate Parameter Estimation on Photovoltaic Modules Using Fisher Information Matrix and D-Optimal Design

STEFANO SCHUBERT[1], (Member, IEEE), VLADIMIR SOVLJANSKI[2], (Member, IEEE), FILIPPO SPERTINO[1], (Senior Member, IEEE), GIANFRANCO CHICCO[1], (Fellow, IEEE), AND MARIO PAOLONE[2], (Fellow, IEEE)

[1]Energy Department, Politecnico di Torino, 10129 Turin, Italy
[2]Distributed Electrical Systems Laboratory, EPFL, 1015 Lausanne, Switzerland

Corresponding author: Stefano Schubert (stefano.schubert@polito.it)

This work was supported in part by Politecnico di Torino through the Italian Project "Dipartimenti di Eccellenza 2023–2027," Department of Energy of Politecnico di Torino, funded by Ministero dell'Universitá e della Ricerca under Grant l. 232/2016, art. 1,-commi 314-337; and in part by École Polytechnique Fédérale de Lausanne through the Swiss Circular Economy Model for Automotive Lithium-Ion Batteries (CircuBAT) Flagship Project, funded by the Swiss Innovation Agency (Innosuisse-Flagship Initiative) under Grant FLAGSHIP PFFS-21-20.

ABSTRACT Accurate estimation of the equivalent circuit parameters of photovoltaic modules enables comprehensive analysis of photovoltaic system's electrical behaviour and facilitates the detection of faults. This paper proposes a rigorous method for optimizing the current-voltage curve measurements by minimizing the variance of the estimated parameters in the typical photovoltaic five-parameter equivalent circuit model. Leveraging the Fisher Information Matrix and the D-optimal experiment design technique, the proposed method aims to improve the accuracy of parameter estimation by optimizing the distribution of current or voltage sampling points, reducing the overall parameter uncertainty as quantified by the determinant of the inverse of Fisher Information Matrix. The study investigates both current and voltage-based sampling approaches, showing that current sampling is preferable under partial shading, while voltage sampling can be equivalently employed under uniform irradiance. The method is validated through both numerical simulations and experimental data from five real photovoltaic modules under both partial shading and uniform irradiance conditions. Experimental validation was conducted on five commercial photovoltaic modules of different technologies, including monocrystalline, polycrystalline, HIT, and TOPCon, confirming that the proposed optimization strategy consistently enhances estimation precision, with variance reductions up to two orders of magnitude.

INDEX TERMS D-optimal design, equivalent circuit model, fisher information matrix, partial shading, photovoltaics Cramér-Rao lower bound.

NOMENCLATURE

CRLB	Cramér–Rao Lower Bound.
DC	Direct Current.
EL	Electronic Load.
FIM	Fisher Information Matrix.
FSR	Full Scale Range.
IID	Independent and Identically Distributed.
I–V	Current–Voltage.
MPP	Maximum Power Point.
PDF	Probability Density Function.
PV	Photovoltaic.
RMSE	Root Mean Square Error.
STC	Standard Test Conditions.
TOPCon	Tunnel Oxide Passivated Contact.
G	Irradiance (W/m^2).
I	Current through the PV module (A).
I_0	Diode saturation current (A).

The associate editor coordinating the review of this manuscript and approving it for publication was Jenny Mahoney.

I_{mpp}	Maximum power point current at STC (A).
I_{ph}	Photogenerated current (A).
I_{sc}	Short Circuit Current (A).
M	Number of parameters (-).
N	Number of measurement points (-).
P_{mpp}	Maximum power point power at STC (W).
R_s	Series resistance (Ω).
R_{sh}	Parallel (shunt) resistance (Ω).
T_c	Cell temperature (K).
V	Voltage across the PV module (V).
V_{mpp}	Maximum power point voltage at STC (V).
V_{oc}	Open circuit voltage (V).
k_b	Boltzmann constant (1.380649×10^{-23} J/K).
n	Diode ideality factor (-).
q	Electron charge ($1.602176634 \times 10^{-19}$ C).
$\mathcal{C}$	Cramér–Rao Lower Bound.
$\mathcal{F}$	Fisher Information Matrix.
$\hat{\theta}$	Estimated parameter vector.
θ	Vector of model parameters.
σ_I^2	Variance of current measurements (A^2).
σ_V^2	Variance of voltage measurements (V^2).
ω_M	Volume of the confidence ellipsoid with M parameters.

I. INTRODUCTION

The growth of photovoltaic (PV) technology as a key component in the global energy transition requires increasingly accurate and efficient methods for monitoring and controlling PV system performance.

Among the most well-known diagnostic and control tools available, the Current–Voltage (I–V) characteristic curve of a PV module provides essential insights into its electrical behaviour and operational state. This curve not only enables real-time monitoring of performance but also serves as the fundamental input for Maximum Power Point Tracking (MPPT) algorithms in grid-connected inverters, thereby directly influencing the energy conversion efficiency and reliability of the PV system.

Accurate acquisition of the I–V curve typically relies on dedicated instruments such as controllable electronic loads, capacitive loads, and DC/DC converters. These devices enable controlled sweeping of voltage or current across the PV module and the recording of the corresponding electrical response with high resolution, typically in the range of 10 mV and 10 mA [1]. The operational bandwidth of such equipment spans from approximately 0.5 Hz to 200 Hz, which is generally adequate for quasi-static characterization of PV modules under stable irradiance conditions [2].

The analytical reproduction of the I–V curve of PV modules requires a grey box mathematical model called equivalent circuit. This model reproduces the I–V curve based on a set of parameters that characterize physical phenomena such as diode recombination, series and shunt resistances, saturation current and photogenerated current. Parameter identification is essential for a variety of applications, including model-based control, fault detection, and performance forecasting.

Importantly, this identification procedure is non-invasive and can be conducted in situ, making it suitable for both laboratory research and field deployment [3].

Among the several modelling approaches, the five-parameter equivalent circuit model is widely adopted due to its favourable trade-off between accuracy and computational burden [4], [5]. This model is capable of accurately capturing the nonlinear I–V behaviour of PV modules under varying environmental and operating conditions.

Recent literature has shown a growing interest in data-driven and optimization-based techniques for PV parameter estimation. The systematic review [6] explores the use of machine learning algorithms in predicting PV system parameters, highlighting their potential for model generalization and fast deployment. Another review provides a comprehensive comparison of analytical, numerical, and heuristic methods, emphasizing their relative accuracy and complexity [7]. Similarly, survey [8] addresses the use of metaheuristic algorithms—such as genetic algorithms and particle swarm optimization—for parameter extraction from I–V curves, demonstrating their flexibility in non-linear optimization scenarios.

Nevertheless, estimating the parameters of the equivalent circuit remains a challenging problem due to the inherent nonlinearity of the governing equations (and the consequent possible multiplicity of identified parameters), their sensitivity to measurement noise, environmental variability, and the initial conditions used in the fitting process [9], [10]. The parameter estimation task is generally formulated as a nonlinear least-squares optimization problem. Traditionally, the Levenberg–Marquardt algorithm has been employed for solving such problems, although heuristic and metaheuristic techniques have also been proposed [11].

To evaluate the quality of the estimated parameters, the Root Mean Square Error (*RMSE*) between the measured and simulated I–V curves is commonly used as a performance metric [8]. However, minimizing *RMSE* alone does not address the fundamental issue of uncertainty quantification in parameter estimation. In this context, estimation theory offers a more rigorous approach relying on the Fisher Information Matrix (FIM), which quantifies the amount of information that the acquired measurements provide about the model parameters.

Maximizing the information content of the measurement data involves the optimal selection of current sample points along the I–V curve. Several strategies from the field of optimal experimental design have been employed for this purpose. Among these, D-optimal design — which maximizes the determinant of the FIM — has proven particularly effective in reducing the overall estimation variance [12]. However, none of the existing literature contribution rigorously addresses optimal I–V curve sampling.

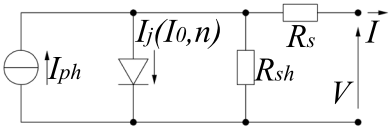

FIGURE 1. PV five parameters model.

This paper addresses a gap in the PV characterization literature by introducing a D-optimal design method for selecting current sample points rather than voltage sample points, that enhance the accuracy of parameter estimation in PV equivalent circuit models. The proposed approach is formulated within the FIM framework and aims to increase the precision of parameter estimates without altering the estimation algorithm itself or assuming specific environmental conditions. Validation is performed through a combination of numerical simulations and experimental tests, including both uniform irradiation and partial shading scenarios.

The main contributions of this paper are as follows:

The remainder of this paper is structured as follows. Section II presents the proposed optimization framework and details the formulation of the estimation problem. Section III discusses the results of numerical simulations and experimental validation. Section IV includes a sensitivity analysis on the number of current points. Section V concludes the work and outlines future research directions.

II. MODEL AND *I–V* CURVE SAMPLING OPTIMIZATION METHOD

A. FIVE PARAMETERS CIRCUIT OF A PV CELL

This work uses the PV cell single-diode five-parameter model (Figure 1). The parameters are included in the vector $\theta = [I_{\text{ph}}, I_0, n, R_{\text{s}}, R_{\text{sh}}]^\top$, in which [13]:

- The photogenerated current I_{ph} represents the current generated by the sunlight incident on the PV module and is directly proportional to the irradiance received.
- The saturation current I_0 is the reverse saturation current of the diode and reflects the leakage current when the PV cell is reverse-biased, with a strong dependence on temperature.
- The diode ideality factor n defines the quality of the diode and represents the deviation from the ideal behaviour, influencing the slope of the I–V curve in the exponential region.
- The series resistance R_{s} accounts for the resistive losses in the connections, contacts, and materials inside the PV cell.
- Lastly, the parallel resistance R_{sh} represents leakage pathways across the PV cell, where lower values lead to greater current losses and a reduction in the open-circuit voltage [14].

Based on the definitions, the current I_{j} that flows into the diode is a function of I_0 and n, $I_{\text{j}} = f(I_0, n)$ These parameters are related through the following non-linear relationship between current and voltage:

$$I_{\text{ph}} - I_0 \cdot \left[\exp\left(\frac{(V + I \cdot R_{\text{s}}) \cdot \text{q}}{n \cdot \text{k}_{\text{b}} \cdot T_{\text{c}}}\right) - 1\right] - \frac{V + I \cdot R_{\text{s}}}{R_{\text{sh}}} - I = 0, \tag{1}$$

where k_{b} is the Boltzmann constant, q is the electron charge, and T_{c} is the absolute cell temperature. Equation (1) embeds the non-linear dependencies between PV cell voltage and current, making parameter estimation a complex task.

B. GENERAL ASSUMPTIONS OF THE PROCEDURE

The assumptions made in this study are as follows:

1) The models of the measurement noise on voltage and current are known and Independent and Identically Distributed (IID).
2) A specific parametric model for the PV cell circuit is utilized and selected a priori by the modeller.
3) The observations/measurements are sufficiently fast to consider the cell temperature T_{c} and irradiance G as a known and noiseless unbiased constant.
4) The method must be applicable for both laboratory and field testing, assuming sufficient solar irradiance in both cases to represent operation under uniform irradiation and partial shading [15].

Although in practical scenarios both temperature and irradiance may be subject to uncertainty, they are treated here as external input parameters rather than decision variables of the estimation problem. Since the proposed method focuses on optimizing the sampling of the electrical variables (voltage and current), the uncertainties in T_c and G lie outside the scope of the optimization framework and cannot be mitigated by the algorithm itself.

Moreover, it is important to note that the acquisition of the full I–V curve typically occurs in less than 100 milliseconds. Within such a short interval, both T_c and G can be reasonably considered constant, thus justifying the assumption to be unbiased and noiseless for the purposes of this analysis.

Let us take sampling points (I, V) in ascending order of current from open circuit to short circuit. Then, the column vector $\mathbf{m}$ represents the equivalent circuit model's expressions for the PV cell voltage and current as functions of the parameters θ, evaluated at the corresponding noiseless voltage V and current I levels, and is defined as:

$$\begin{aligned}\mathbf{m} = [&I_1(\theta, \boldsymbol{v}), V_1(\theta, \boldsymbol{i}), \ldots, \\ &I_i(\theta, \boldsymbol{v}), V_i(\theta, \boldsymbol{i}), \ldots, \\ &I_N(\theta, \boldsymbol{v}), V_N(\theta, \boldsymbol{i})]^\top.\end{aligned} \tag{2}$$

Likewise, the vector $\tilde{\mathbf{m}} = [\tilde{I}_1, \tilde{V}_1, \ldots, \tilde{I}_i, \tilde{V}_i, \ldots, \tilde{I}_N, \tilde{V}_N]^\top$ contains the measured voltages and currents at the N data points of the I–V curve. The estimated parameters included in the vector of the PV cell circuit are $\hat{\theta} = [\hat{I_{\text{ph}}}, \hat{I}_0, \hat{n}, \hat{R}_{\text{s}}, \hat{R_{\text{sh}}}]^\top$ and are obtained by solving a standard-least square optimization problem [4], where user defined bounds are imposed on the parameters to be identified. The specific values for

the upper boundary θ_{max} and lower boundary θ_{min} of these constraints may be derived from the literature. Reflecting the IID assumption on measurements, the discrepancies between the measured and modelled values are weighted using the inverse of the measurement covariance matrix $\tilde{\boldsymbol{Q}}$, structured in a block-diagonal form $\tilde{\boldsymbol{Q}} = \text{diag}(\tilde{\boldsymbol{Q}}_1, \ldots, \tilde{\boldsymbol{Q}}_i, \ldots, \tilde{\boldsymbol{Q}}_N)$, where $\tilde{\boldsymbol{Q}} = \text{diag}\left(\sigma_V^2, \sigma_I^2\right)$, as detailed in Section II-C.

The equation used to estimate $\hat{\theta}$ can be represented in the standard quadratic form as follows:

$$\begin{aligned} \hat{\theta} &= \arg\min_{\theta} \left(\tilde{\mathbf{m}} - \mathbf{m}\right)^{\top} \tilde{\boldsymbol{Q}}^{-1} \left(\tilde{\mathbf{m}} - \mathbf{m}\right), \\ \text{s.t.} \quad & \theta_{min} \leq \theta \leq \theta_{max} \end{aligned} \tag{3}$$

C. PROBABILISTIC METROLOGY ASPECTS

As in [16], the Fisher information needs to be derived. The main requirement is to know the noise model distribution, assumed to be Gaussian.

Using commercial measurement instruments, the datasheet typically specifies the uncertainty in the voltage (Δ_V) and current (Δ_I) readings as a percentage of the FSR (Full Scale Range). To determine the variance of the voltage (σ_V^2) and current (σ_I^2) measurements, the three-sigma rule is commonly applied. This common rule states that the unbiased measurement error lies within a probability range of 99.73%. To compute the standard deviation from this error, one can simply divide the FSR error by 3, leading to the constant values $\sigma_V = \frac{1}{3}\Delta_V$ and $\sigma_I = \frac{1}{3}\Delta_I$.

The matrix $\tilde{\boldsymbol{Q}}_i$ is then formed with two constant entries and is represented as $\tilde{\boldsymbol{Q}}_i = \text{diag}(\sigma_V^2, \sigma_I^2),\ \forall\, i = 1, \ldots, N$.

The minimization problem is then formulated as follows for the N measurements:

$$\hat{\theta} = \arg\min_{\theta} \sum_{i=1}^{N} \left(\left(\begin{bmatrix} \tilde{I}_i \\ \tilde{V}_i \end{bmatrix} - \begin{bmatrix} I_i(\theta, V) \\ V_i(\theta, I) \end{bmatrix} \right)^{\top} \cdot \tilde{\boldsymbol{Q}}_i^{-1} \cdot \left(\begin{bmatrix} \tilde{I}_i \\ \tilde{V}_i \end{bmatrix} - \begin{bmatrix} I_i(\theta, V) \\ V_i(\theta, I) \end{bmatrix} \right) \right) \tag{4}$$

D. DERIVATION OF THE CRAMÉR-RAO LOWER BOUND IN VIEW OF PV EQUIVALENT CIRCUIT PARAMETERS

To determine the quality of the PV equivalent circuit parameter estimation, it is necessary to define the minimum theoretical variance. This can be computed by means of the Cramér-Rao Lower Bound (CRLB). This section describes the theoretical derivation of CRLB for the specific problem.

Let $\mathbf{d}_{\theta,\mathbf{v}} = \tilde{\mathbf{i}} - \mathbf{i}(\theta, \mathbf{v})$ and $\mathbf{d}_{\theta,\mathbf{i}} = \tilde{\mathbf{v}} - \mathbf{v}(\theta, \mathbf{i})$ denote the residual vectors that quantify the differences between measurements and model predictions at voltage $\mathbf{v}$ and current $\mathbf{i}$. Let $\mathcal{I}$ and $\mathcal{V}$ denote the random vectors corresponding to the measured current and voltage samples, respectively. The Gaussian PDF of the measurement errors is defined by the following expressions:

$$\text{PDF}(\mathcal{V}|\theta, \boldsymbol{i}) = \frac{1}{\sqrt{(2\pi)^N \det \tilde{\boldsymbol{Q}}}} \cdot \exp\left[-\frac{1}{2}\mathbf{d}_{\theta,\mathbf{i}}^{\top} \tilde{\boldsymbol{Q}}^{-1} \mathbf{d}_{\theta,\mathbf{i}}\right], \tag{5}$$

$$\text{PDF}(\mathcal{I}|\theta, \boldsymbol{v}) = \frac{1}{\sqrt{(2\pi)^N \det \tilde{\boldsymbol{Q}}}} \cdot \exp\left[-\frac{1}{2}\mathbf{d}_{\theta,\mathbf{v}}^{\top} \tilde{\boldsymbol{Q}}^{-1} \mathbf{d}_{\theta,\mathbf{v}}\right]. \tag{6}$$

This formulation allows for the derivation of the log-likelihood function L, which can be expressed as:

$$\begin{aligned} L(\theta, \boldsymbol{i}|\mathcal{V}) &= \ln \text{PDF}(\mathcal{V}|\theta, \boldsymbol{i}), \\ L(\theta, \boldsymbol{v}|\mathcal{I}) &= \ln \text{PDF}(\mathcal{I}|\theta, \boldsymbol{v}). \end{aligned} \tag{7}$$

$$\begin{aligned} L(\theta, \boldsymbol{i}|\mathcal{V}) &= -\frac{N}{2}\ln 2\pi - \frac{1}{2}\ln\det\tilde{\boldsymbol{Q}} - \frac{1}{2}\boldsymbol{d}_{\theta,\boldsymbol{i}}^{\top}\tilde{\boldsymbol{Q}}^{-1}\boldsymbol{d}_{\theta,\boldsymbol{i}}, \\ L(\theta, \boldsymbol{v}|\mathcal{I}) &= -\frac{N}{2}\ln 2\pi - \frac{1}{2}\ln\det\tilde{\boldsymbol{Q}} - \frac{1}{2}\boldsymbol{d}_{\theta,\boldsymbol{v}}^{\top}\tilde{\boldsymbol{Q}}^{-1}\boldsymbol{d}_{\theta,\boldsymbol{v}}. \end{aligned} \tag{8}$$

To determine the first-order partial derivatives with respect to each parameter θ_j, where $j = 1, \ldots, M$, being M the number of parameters to be identified:

$$\begin{aligned} \frac{\partial L(\theta, \boldsymbol{i}|\mathcal{V})}{\partial \theta_j} &= -\frac{1}{2}\frac{\partial}{\partial\theta_j}\ln\det\tilde{\boldsymbol{Q}} - \frac{1}{2}\frac{\partial}{\partial\theta_j}\left(\boldsymbol{\epsilon}^{\top}(\theta, \boldsymbol{i})\tilde{\boldsymbol{Q}}^{-1}\boldsymbol{d}_{\theta,\boldsymbol{i}}\right) \\ &= -\frac{1}{2}\text{trace}\left(\tilde{\boldsymbol{Q}}^{-1}\frac{\partial\tilde{\boldsymbol{Q}}}{\partial\theta_j}\right) + \frac{\partial\boldsymbol{\epsilon}^{\top}(\theta, \boldsymbol{i})}{\partial\theta_j}\tilde{\boldsymbol{Q}}^{-1}\boldsymbol{d}_{\theta,\boldsymbol{i}} \\ &\quad - \frac{1}{2}\boldsymbol{\epsilon}^{\top}(\theta, \boldsymbol{i})\tilde{\boldsymbol{Q}}^{-1}\frac{\partial\tilde{\boldsymbol{Q}}}{\partial\theta_j}\tilde{\boldsymbol{Q}}^{-1}\boldsymbol{d}_{\theta,\boldsymbol{i}}, \end{aligned} \tag{9}$$

$$\begin{aligned} \frac{\partial L(\theta, \boldsymbol{v}|\mathcal{I})}{\partial \theta_j} &= -\frac{1}{2}\frac{\partial}{\partial\theta_j}\ln\det\tilde{\boldsymbol{Q}} - \frac{1}{2}\frac{\partial}{\partial\theta_j}\left(\boldsymbol{\epsilon}^{\top}(\theta, \boldsymbol{v})\tilde{\boldsymbol{Q}}^{-1}\boldsymbol{d}_{\theta,\boldsymbol{v}}\right) \\ &= -\frac{1}{2}\text{trace}\left(\tilde{\boldsymbol{Q}}^{-1}\frac{\partial\tilde{\boldsymbol{Q}}}{\partial\theta_j}\right) + \frac{\partial\boldsymbol{\epsilon}^{\top}(\theta, \boldsymbol{v})}{\partial\theta_j}\tilde{\boldsymbol{Q}}^{-1}\boldsymbol{d}_{\theta,\boldsymbol{v}} \\ &\quad - \frac{1}{2}\boldsymbol{\epsilon}^{\top}(\theta, \boldsymbol{v})\tilde{\boldsymbol{Q}}^{-1}\frac{\partial\tilde{\boldsymbol{Q}}}{\partial\theta_j}\tilde{\boldsymbol{Q}}^{-1}\boldsymbol{d}_{\theta,\boldsymbol{v}}. \end{aligned} \tag{10}$$

Since $\tilde{\boldsymbol{Q}}$ is constant, the trace is null in (9) and (10). Therefore, (9) and (10) become:

$$\frac{\partial L(\theta, \boldsymbol{i}|\mathcal{V})}{\partial\theta_j} = \frac{\partial\boldsymbol{\epsilon}^{\top}(\theta, \boldsymbol{i})}{\partial\theta_j}\tilde{\boldsymbol{Q}}^{-1}\boldsymbol{d}_{\theta,\boldsymbol{i}}, \tag{11}$$

$$\frac{\partial L(\theta, \boldsymbol{v}|\mathcal{I})}{\partial\theta_j} = \frac{\partial\boldsymbol{\epsilon}^{\top}(\theta, \boldsymbol{v})}{\partial\theta_j}\tilde{\boldsymbol{Q}}^{-1}\boldsymbol{d}_{\theta,\boldsymbol{v}}. \tag{12}$$

Let us denote the FIM as the matrix $\boldsymbol{\mathcal{F}} \in \mathbb{R}^{M\times M}$. The (k, ℓ)-th entry of $\boldsymbol{\mathcal{F}}$ is defined as a function of the parameter vector θ, where $\mathbb{E}$ denotes the expected value of the product of the partial derivatives of the log-likelihood function with respect to the k-th and ℓ-th parameters:

$$\boldsymbol{\mathcal{F}}(\theta)_{k,\ell} = \mathbb{E}\left[\frac{\partial L(\theta, \boldsymbol{i}|\mathcal{V})}{\partial\theta_k}\cdot\frac{\partial L(\theta, \boldsymbol{i}|\mathcal{V})}{\partial\theta_\ell} + \frac{\partial L(\theta, \boldsymbol{v}|\mathcal{I})}{\partial\theta_k}\cdot\frac{\partial L(\theta, \boldsymbol{v}|\mathcal{I})}{\partial\theta_\ell}\right]. \tag{13}$$

The expression of the (k, ℓ)-th element of the FIM can be rewritten in compact form in the following way [17]:

$$\mathcal{F}(\theta)_{k,\ell} = +\frac{1}{\sigma_I^2}\sum_{i=1}^{N}\frac{\partial I(\theta, V_i)}{\partial \theta_k}\frac{\partial I(\theta, V_i)}{\partial \theta_\ell} + \frac{1}{\sigma_V^2}\sum_{i=1}^{N}\frac{\partial V(\theta, I_i)}{\partial \theta_k}\frac{\partial V(\theta, I_i)}{\partial \theta_\ell}. \quad (14)$$

The element (k, ℓ) of the FIM, can be expressed as the sum of contributions at every sampled voltage $V_i, i = 1, \ldots, N$. It is worth reminding that the N voltage measurements are, for simplicity, sorted in ascending order.

$$\mathcal{F}(\theta)_{k,\ell} = \sum_{i=1}^{N}\Delta\mathcal{F}_i(\theta)_{k,\ell}. \quad (15)$$

Each measured data point provides different information for each parameter θ_j, contributing to the FIM [17]. The contribution to the FIM element (k, ℓ) can be represented as a function dependent on θ, V and I:

$$\Delta\mathcal{F}(\theta)_{k,\ell} = +\frac{1}{\sigma_I^2}\frac{\partial I(\theta, V)}{\partial \theta_k}\frac{\partial I(\theta, V)}{\partial \theta_\ell} + \frac{1}{\sigma_V^2}\frac{\partial V(\theta, I)}{\partial \theta_k}\frac{\partial V(\theta, I)}{\partial \theta_\ell}. \quad (16)$$

The computation of the CRLB requires to evaluate the elements of the FIM at the true parameter values θ^* which in practice are not known.[1] The FIM, when evaluated at these true parameters, is represented as $\mathcal{F}^*$:

$$\mathcal{F}^*_{k,\ell} = \mathcal{F}(\theta)_{k,\ell}\Big|_{\theta=\theta^*}. \quad (17)$$

The inverse of the FIM, evaluated at the true parameter, yields the CRLB $:= \mathcal{F}^{*-1}$. The CRLB can finally be used as the benchmark to define the minimum theoretical variance of θ;

$$\sigma^2_{\theta_i} := \mathrm{Var}(\theta_i) \geq \mathcal{F}^{*-1}_{i,i}, \quad \forall i = 1, \ldots, M. \quad (18)$$

E. LEAST-VARIANCE CIRCUIT PARAMETER IDENTIFICATION VIA CRLB

This section introduces the algorithm designed to identify a set of voltages (considered as decision variables) that yield measurements containing the most informative data for estimating the PV parameters. This is achieved by maximizing the determinant of the FIM with the method known as D-optimal experiment design.

The square matrix $\mathcal{F}$ is by construction real, symmetric, invertible, and positive-semidefinite. As such, it possesses M real, non-negative eigenvalues, and its determinant is positive, denoted by $\det(\mathcal{F}) \geq 0$.

Maximising the determinant of $\mathcal{F}$ minimizes the determinant of $\mathcal{F}^{-1}$, as one is the inverse of the other.

[1] Section III-C shows how to deal with this issue.

Furthermore, minimizing the determinant of $\mathcal{F}^{-1}$ results in the smallest possible volume of the confidence ellipsoid ω_M for estimating the M parameters [17].

$$\omega_M = \frac{2}{M}\frac{\pi^{M/2}}{\Gamma\left(\frac{M}{2}\right)}\frac{1}{\sqrt{\det(\mathcal{F})}}, \quad (19)$$

where Γ represents the Gamma function.

A smaller ellipsoid volume, ω_M, signifies an overall enhancement in the precision of the parameter estimates. While some standard deviations, e.g., for the j^{th} parameter $\sigma^2_{\theta_j}$, may increase and others may decrease, the net effect is a reduction in ω_M, indicating improved accuracy in the estimation process of $\hat{\theta}$.

F. ALGORITHM FOR CURRENT SAMPLING ADJUSTMENTS VIA D-OPTIMAL DESIGN

The goal of Algorithm 1 is to modify the current sampling points such that the resulting current sampling distribution yields more accurate parameter estimates than those obtained using the conventional uniformly spaced current span for the same predetermined number of sampled points N. The initial and optimized current selections are $\mathbf{i}_{\text{init}} \in \Re$ and $\mathbf{i}_{\text{opt}} \in \Re$, respectively, and cover the same current range $[0, I_{sc}]$.

The procedures in Algorithm 1 are given here below.

- `GenerateIVCurve` simulates the I–V curve with added noise to facilitate realistic parameter estimation and optimization. It takes as inputs the ground truth parameter set θ^* (as indicated in Section III-C), the open short circuit current I_{sc}, the desired number of points N in the current sample, and the variances of voltage and current, σ_V^2 and σ_I^2, respectively. The procedure generates a uniformly spaced array of current values ranging from 0 to I_{sc}, for I–V curve simulation. Using the five-parameter I–V model function `IVModel`, the procedure calculates the corresponding noiseless voltage values $\mathbf{v}$ based on the ground truth parameters. Gaussian noise is then introduced into both the current and voltage values to yield the arrays $\mathbf{i}_{\text{noise}}$ and $\mathbf{iv}_{\text{noise}}$, which represent the noisy observations. Finally, the procedure returns the noisy voltage and current arrays, $\mathbf{i}_{\text{noise}}$ and $\mathbf{v}_{\text{noise}}$, for use in subsequent processes. If the I–V curve is generated starting from the voltage values, the role of $\mathbf{i}$ and $\mathbf{v}$ is swapped.
- `EstimateParameters` initializes the parameter estimation process by taking voltage and current data, voltage variance σ_V^2, current variance σ_I^2, and an initial guess for the parameters as inputs. The procedure defines the estimated parameter values and the optimized current sample distribution as outputs. Using equation (3), it estimates the equivalent circuit parameters from the noisy I–V measurements, calculating the variance for each parameter [18]. In this work, the Levenberg-Marquardt algorithm is employed as the numerical solver for the nonlinear least-squares problem.

Algorithm 1 Current Sampling Distribution Optimization Using D-Optimal Design

Input: Number of parameters N, Noisy voltage and current data $\mathbf{v}_{\text{noise}}$, $\mathbf{i}_{\text{noise}}$, Voltage and current variances σ_V^2, σ_I^2, Initial guess θ_{init}
Output: Estimated parameters $\hat{\theta}$, Optimized current sampling vector $\mathbf{i}_{\text{opt}}$

Procedure: MAIN(N, $\mathbf{v}_{\text{noise}}$, $\mathbf{i}_{\text{noise}}$, σ_V^2, σ_I^2, θ_{init})
/* These are inputs only when the optimization is performed on real measurements. When the measurements are synthetic, the procedure GenerateIVCurve is used. */
$\theta_{\text{est}}, \sigma_{\text{est}}^2 \leftarrow$ EstimateParameters($\mathbf{v}_{\text{noise}}, \mathbf{i}_{\text{noise}}$)
$\mathbf{v}_{\text{opt}}, \mathbf{i}_{\text{opt}} \leftarrow$ OptCurrentDist($\mathbf{i}_{\text{init}}, \theta_{\text{est}}, \sigma_V^2, \sigma_I^2$)
$\hat{\theta}, \sigma_{\text{opt}}^2 \leftarrow$ EstimateParameters($\mathbf{v}_{\text{noise\_opt}}, \mathbf{i}_{\text{noise\_opt}}$)
return $\hat{\theta}$, $\mathbf{i}_{\text{opt}}$

Procedure: GENERATEIVCURVE(θ^*, V_{oc}, N, σ_V^2, σ_I^2, T_c)
/* Generate current sample selection */
$\mathbf{i} \leftarrow$ sampling(0, I_{sc}, N)
/* Compute noiseless voltage values */
$\mathbf{v} \leftarrow$ IVModel($\mathbf{i}$, θ^*, T_c)
/* Corrupt voltage with Gaussian independent noise */
$\mathbf{v}_{\text{noise}} \leftarrow \mathbf{v} + \text{normal}(0, \sigma_V^2)$
/* Corrupt current with Gaussian independent noise */
$\mathbf{i}_{\text{noise}} \leftarrow \mathbf{i} + \text{normal}(0, \sigma_I^2)$
return $\mathbf{v}_{\text{noise}}$, $\mathbf{i}_{\text{noise}}$

Procedure: ESTIMATEPARAMETERS($\mathbf{v}_{\text{noise}}, \mathbf{i}_{\text{noise}}$)
/* θ_{est} is the tuple of estimated parameters, and Σ_{est} is the estimated approximate covariance matrix of θ_{est}. The diagonal elements of Σ_{est} provide the variance of the parameter estimates σ_{est}^2. */
$\theta_{\text{est}}, \Sigma_{est} \leftarrow$ curve_fit(IVModel, $\mathbf{v}_{\text{noise}}, \mathbf{i}_{\text{noise}}, \theta_{\text{init}}$)
$\sigma_{\text{est}}^2 \leftarrow \text{diag}(\Sigma_{est})$
return θ_{est}, σ_{est}^2

Procedure: COMPUTEFIM($\mathbf{v}_{\text{noise}}, \mathbf{i}_{\text{noise}}, \theta_{\text{est}}$)
FIM $\leftarrow$ FisherInformationMatrix($\mathbf{v}_{\text{noise}}, \mathbf{i}_{\text{noise}}, \theta_{\text{est}}$)
CRLB $\leftarrow$ diag(inv(*FIM*))
return *FIM*, *CRLB*

Procedure: OBJECTIVEFUNCTION($\mathbf{v}_{\text{noise}}, \theta_{\text{est}}$)
FIM $\leftarrow$ ComputeFIM($\mathbf{v}_{\text{noise}}, \mathbf{i}_{\text{noise}}, \theta_{\text{est}}$)
/* Objective function: $-\log(\det(FIM))$ */
return $-\log(\det(FIM))$

Procedure: OPTCURRENTDIST($\mathbf{i}_{\text{init}}, \theta_{\text{est}}, \sigma_V^2, \sigma_I^2$)
/* Initialize an empty array to store variances */
variances $\leftarrow$ [ ]
while not converged **do**
  /* Estimate parameters for the iteration */
  $\theta_{\text{iter}} \leftarrow$ EstimateParameters(θ_{est})
  /* Estimate the variance of the estimated parameters */
  $\sigma_{\text{iter}}^2 \leftarrow$ estimateVariance($\theta_{\text{iter}}, \sigma_V^2, \sigma_I^2$)
  /* Store the variance in the array */
  add(σ_{iter}^2, variances)
  /* Optimize for the current iteration */
  $\mathbf{i}_{\text{opt}} \leftarrow$ MinimizeIteration(ObjectiveFunction, $\mathbf{i}_{\text{init}}, \theta_{\text{iter}}, \sigma_V^2, \sigma_I^2$)
end while
/* Return the optimized current selection and the array of variances */
return $\mathbf{i}_{\text{opt}}$, variances

- ComputeFIM computes the FIM using the estimated parameters from the initial data and the noisy voltage and current observations, based on Equation (14). The diagonal of the inverse of the FIM provides the CRLB, giving an estimate of the lower bound of parameter variance [19].
- ObjectiveFunction defines the objective function for optimization, using the FIM obtained from ComputeFIM. The objective function is calculated as the negative of the log-determinant of the FIM, as per Equation (14), which is instrumental in guiding the optimization process by minimizing the parameter variance.

- `OptCurrentDist` performs the iterative optimization of the current sample distribution using a minimization function. In each iteration, it estimates the parameters, calculates their variance, and stores this variance in an array. The optimized current sample distribution and the array of variances are returned, offering insights into the convergence of parameter estimates during optimization.
- `Main` coordinates the overall process as follows:
  - It first calls `EstimateParameters` to perform an initial parameter estimation from the unoptimized current sample distribution.
  - Next, it calls `OptCurrentDist` to optimize the current sample distribution.
  - Finally, it calls `EstimateParameters` a second time on the optimized distribution to refine the parameter estimates.
  - The function returns the final optimized parameters and the optimized current sample distribution.

III. APPLICATION OF THE METHOD TO PV MODULES

This section presents the application of the method described in Section II. The application is divided in three parts:

1) A description of the topology of commercial PV modules.
2) Numerical simulations in which I–V data are generated in a synthetic manner.
3) Experiments in which a real PV module has been tested while in operation.

A. CONFIGURATION OF HALF CELLS PV MODULES

Modern PV modules frequently adopt a half-cell configuration, wherein each full-size cell is physically sliced into two equal halves to reduce resistive losses and improve thermal behaviour [20]. In this configuration, each substring comprises two identical branches of half-cells connected in parallel, effectively, under uniform irradiance, halving the operating current in each branch compared to conventional full-cell designs. Within each branch, the half-cells are connected in series.

Typically, a PV module consists of three or four such substrings connected in series, with each substring protected by an individual bypass diode to mitigate power losses under partial shading conditions. Figure 2 illustrates the electrical topology of a modern PV module composed of half-cell arranged into three submodules, one per bypass diode. These submodules are referred to as *strings* for the rest of this paper. Each of these strings comprises two series-connected half-cell groups, forming a layout commonly adopted in high-efficiency PV modules to reduce resistive losses.

The I–V characteristics depicted in Figure 2 compare two operating scenarios. The orange curve corresponds to the ideal case of uniform irradiance, in which all strings receive full illumination and the bypass diodes remain inactive. In contrast, the blue curve shows the characteristic multi-step

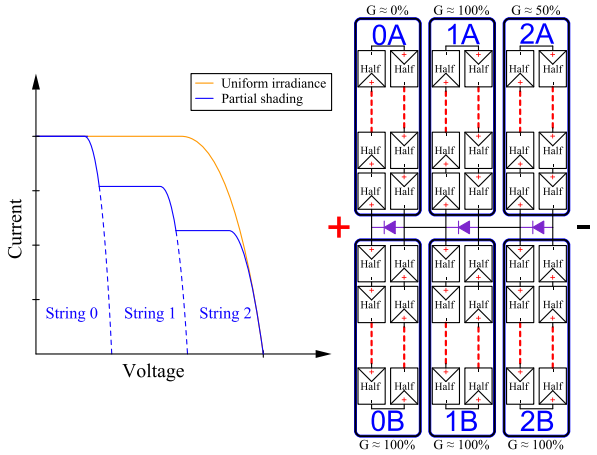

FIGURE 2. Usual topology of a half cells PV module and its *I–V* curve.

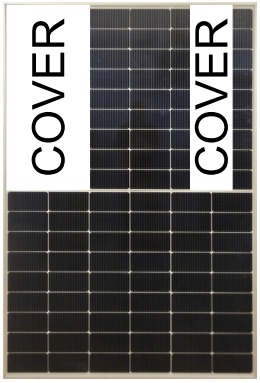

FIGURE 3. Partial shading pattern on the HT54-18XN-435 half cells PV module.

behaviour that emerges under partial shading conditions due to the sequential activation of bypass diodes.

In the partial shading configuration associated with the blue curve, all strings are uniformly illuminated except for two critical regions: the string labelled `2A`, which receives approximately 50% of the nominal irradiance, and the string `0A`, which is completely shaded. These shading conditions result in the activation of the respective bypass diodes, effectively clipping the contribution of the affected strings to maintain the overall module current. This operational behaviour produces the three-step voltage profile shown in the blue I–V trace.

The exact implementation of this irradiance pattern on a commercial PV module is illustrated in Figure 3, which shows the physical masking of the corresponding areas. Specifically, partial coverage is applied to the region corresponding to `2A`, while complete coverage is applied to the region corresponding to `0A`, as indicated by the labelled "COVER" masks. This controlled shading enables experimental reproduction of the non-uniform irradiance profile necessary for the validation of shade-aware modelling techniques. Additional photographs that illustrate the applied

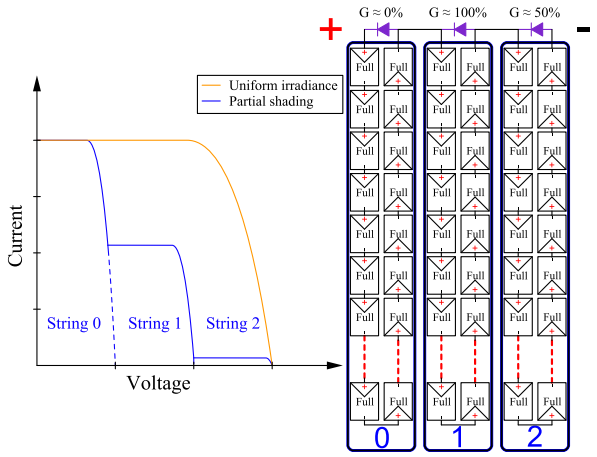

FIGURE 4. Electrical configuration and *I–V* response of a full-cell PV module with three substrings under partial shading.

shading conditions for the other tested modules are included in Section III-D for clarity and reproducibility.

As illustrated in the topology, bypass diodes are integrated across each one of the three substrings in an anti-parallel configuration. These diodes allow current to bypass individual substrings in the event of partial shading, physical damage, or mismatch, thereby preventing localized overheating (hotspot formation) and preserving the energy yield of the module.

In PV modules featuring series-connected substrings with internal parallel branches—such as those employing a half-cell architecture, the most suitable approach for characterizing the I–V curve involves imposing the current and measuring the corresponding voltage response. This measurement strategy is particularly advantageous given the internal topology, wherein each substring consists of parallel-connected branches of series-linked cells.

A comparison can be made with standard full-cell modules, which do not use internal parallelization within substrings. In these modules, each cell is full-sized, and substrings are made of a single series chain of such cells. Bypass diodes are typically installed across each substring to ensure energy yield under mismatch or shading. The electrical topology and corresponding I–V curve under partial shading conditions for this type of module is illustrated in Figure 4.

As shown, the three substrings labelled 0, 1, and 2 are electrically connected in series and protected by bypass diodes. In this setup, substring 0 receives full irradiance ($G = 100\%$), substring 1 is partially shaded ($G \approx 50\%$), and substring 2 is fully shaded ($G \approx 0\%$), with small current output from diffuse irradiance.

This specific shading condition causes a stepwise behaviour in the I–V curve similar to that observed in half-cell modules, although the shape is influenced by the absence of internal current sharing through parallel branches.

In this topology, current-based sampling is also preferable when characterizing the module under partial shading. By controlling the current imposed on the entire module, the activation of individual bypass diodes can be correctly captured, and the contribution of each substring to the overall module response can be separately analysed.

B. ALGORITHM FOR GENERATION OF SYNTHETIC DATA

The procedure `GenerateIVCurve` (Algorithm 2) is used with the primary objective of generating synthetic noisy I–V data that mimic real I–V curves. As explained in Section II, σ_I^2 and σ_V^2 depend on the metrological characteristics of the current and voltage probes. It is possible to model this metrological aspect of the I–V curve by introducing Gaussian noise into the voltage and current observations. This enables testing and validation of the current adjustment algorithm for estimating PV parameters prior to deployment in real-world conditions. By replicating measurement noise typically encountered in practice, the procedure ensures that parameter estimation and current sample selection optimization remain accurate and robust.

In addition to modelling noise, the procedure explicitly accounts for partial shading conditions within the PV module. This is achieved by imposing the current and computing the voltage response for each one of the three strings of the module individually, using the five-parameter model, with a distinct set of parameters for each string. For a given current value, the voltages of the three strings are computed and summed up, and the forward voltage drop of the bypass diode is subtracted from the total. This effectively models the bypassing behaviour and allows each string to be treated as an independent electrical unit contributing to the overall module response.

This approach enables the simulation of PV modules composed of any number of strings by extending the procedure accordingly and assigning independent parameters to each string. If the parameter sets are identical across all strings, the model simulates ideal conditions such as uniform irradiance on a sunny day. On the other hand, introducing variations among the string parameters allows simulation of mismatch effects caused by partial shading, dirt accumulation, or other non-uniformities.

The contents of Algorithm 2 are explained as follows, considering the example of a three-string PV module as in Figure 2.

- Line 2: The procedure `GenerateIVCurve` is defined with the following inputs: three parameter sets θ_0, θ_1, and θ_2 representing the five-parameter model configurations for each one of the three strings of the PV module; I_{sc}, the short-circuit current used to define the range of simulation; T, the cell temperature (used for thermal voltage calculation); n_{meas}, the number of samples; σ_V and σ_I, the standard deviations of the voltage and current noise, respectively
- Line 3: A uniformly spaced array of current values $\mathbf{i}$ is generated, ranging from 0 to I_{sc}, with a total of n_{meas}

Algorithm 2 Generation of Synthetic Noisy I–V Curves Under Partial Shading

1: **Procedure:** GENERATEIVCURVE()
2: **Input:** $\theta = \{\theta_0, \theta_1, \theta_2\}$, I_{sc}, T, n_{meas}, σ_V, σ_I
3: $\mathbf{i} \leftarrow \text{linspace}(0, I_{sc}, n_{points})$
4: **for** $j \in \{0, 1, 2\}$ **do**
5: $\mathbf{v}_j \leftarrow \texttt{IVModel}(\mathbf{i}, \theta_j) \cdot N_s - V_{f,j}$
6: Set $\mathbf{v}_j \leftarrow$ NaN where $\mathbf{v}_j < 0$
7: **end for**
8: $\mathbf{v} \leftarrow \mathbf{v}_0 + \text{fillna}(\mathbf{v}_1, 0) + \text{fillna}(\mathbf{v}_2, 0)$
9: /* Add voltage noise */
10: $\mathbf{v} \leftarrow \mathbf{v} + \text{normal}(0, \sigma_V)$
11: /* Add current noise */
12: $\mathbf{i} \leftarrow \mathbf{i} + \text{normal}(0, \sigma_I)$
13: **return** $\mathbf{v}, \mathbf{i}$

points. This array represents the independent variable for which voltage values are computed.

- Lines 4–7: For each string $j = \{0, 1, 2\}$, the voltage response $\mathbf{v}_j$ is computed by evaluating the five-parameter model function `IVModel` using the corresponding parameter set θ_j and the current array $\mathbf{i}$. The result is scaled by N_s to account for the number of cells in series and then the forward voltage of the bypass diode $V_{f,j}$ is subtracted, if necessary. Any resulting negative voltages (non-physical) are masked by assigning them as NaN (not-a-number) values.
- Line 8: The final voltage array $\mathbf{v}$ is computed by summing the per-string voltage contributions. Missing (NaN) values from partially shaded strings are replaced with zeros using a fill-in operation. This summation emulates the behaviour of strings operating in parallel with bypass diodes under partial shading.
- Line 10: Using a SciPy library function [21], Gaussian noise with standard deviation σ_V is added to the voltage array. The noise simulates measurement uncertainty in the voltage readings.
- Line 12: Similarly, Gaussian noise with standard deviation σ_I is added to the current values, modelling uncertainty in the current measurement.
- Line 13: The procedure returns the arrays $\mathbf{v}$ and $\mathbf{i}$, now representing synthetic I–V data that include realistic noise and partial shading effects. These outputs can be used to evaluate the performance of parameter estimation algorithms under simulated field conditions.

C. NUMERICAL SIMULATION

In the five-parameter equivalent circuit equation, the ground truth parameters are defined as $\theta^* = [I^*_{ph}, \log(I_0)^*, n^*, R^*_s, R^*_{sh}]$ and their numerical values, for each string, are summarized in Table 1.

The inputs consist of the known, unbiased, and noiseless cell temperature T_c (K), along with the uniformly spaced noiseless current sample selection in the range $[0, I_{sc}]$.

TABLE 1. Ground truth parameters.

Case	String	I_{ph} (A)	$\log(I_0)$ (-)	n (-)	R_s (mΩ)	R_{sh} (Ω)
Partial shading	0	10	-18	1.35	1	2
	1	7	-13	1.6	5	2
	2	5	-12	1.6	5	2
Uniform irradiation	0	10	-18	1.35	1	2
	1	10	-18	1.35	1	2
	2	10	-18	1.35	1	2

TABLE 2. Numerical inputs used in the simulation.

I_{sc}, (A)	T_c (°C)	σ^2_V (V^2)	σ^2_I (A^2)
10.0	40.0	1e-4	2.56e-2

To simulate the noiseless I–V characteristics of the PV module, the explicit formulation of the five-parameter equivalent circuit model is employed. Depending on whether the current or voltage is treated as the independent variable, two different expressions can be employed.

When the current is selected as the input, the corresponding voltage can be computed explicitly using the following equation, where W(·) denotes the Lambert W function [22]:

$$V = -I \cdot R_s - I \cdot R_{sh} + \exp(\log(I_0)) \cdot R_{sh} + I_{ph} \cdot R_{sh} - \left(\frac{n \cdot k_B \cdot T_c}{q}\right) \cdot \mathrm{W}\left(\frac{\exp(\log(I_0)) \cdot R_{sh} \cdot \exp\left(\frac{R_{sh} \cdot (-I + \exp(\log(I_0)) + I_{ph})}{\left(\frac{n \cdot k_B \cdot T_c}{q}\right)}\right)}{\left(\frac{n \cdot k_B \cdot T_c}{q}\right)}\right). \tag{20}$$

Conversely, when the voltage is chosen as the input variable, the cell current can be calculated using the following explicit expression:

$$I = \frac{I_{ph} + \exp(\log(I_0)) - \frac{V}{R_{sh}}}{1 + \frac{R_s}{R_{sh}}} - \frac{\frac{n \cdot k_B \cdot T_c}{q}}{R_s} \cdot \mathrm{W}\left(\frac{R_s \exp(\log(I_0))}{\frac{n \cdot k_B \cdot T_c}{q}\left(1 + \frac{R_s}{R_{sh}}\right)} \exp\left(\frac{R_s(I_{ph} + \exp(\log(I_0))) + V}{\frac{n \cdot k_B \cdot T_c}{q}\left(1 + \frac{R_s}{R_{sh}}\right)}\right)\right). \tag{21}$$

The procedure `GenerateIVCurve` simulates the observations $\tilde{\mathbf{v}}_{\text{init}}$ and $\tilde{\mathbf{i}}_{\text{init}}$. To calculate the FIM and CRLB, it is still necessary to know σ^2_V and σ^2_I. Values corresponding to a typical measurement system have been chosen. Table 2 shows the numerical values.

As discussed in Section II-D, each parameter yields a different quantity of information at each voltage measurement.

Figure 5 shows the normalized contribution to the diagonal elements of the FIM. These contributions, computed as $[\Delta\mathcal{F}]_{kk}$ using Equation (16), are evaluated over the entire

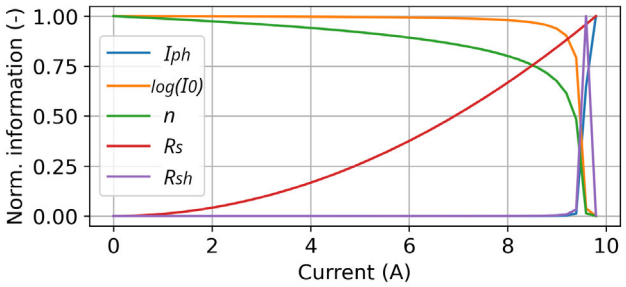

FIGURE 5. Normalized FIM information of each parameter in function of current.

range of $\tilde{\mathbf{v}}$ and $\tilde{\mathbf{i}}$. In this case, the contributions correspond to the parameters of one of the three strings in partially shaded conditions.

In this analysis, the voltage and current noise variances are assumed to be known and uncorrelated. While this reflects the idealized assumption of IID Gaussian noise, it is important to acknowledge that real-world measurement noise may deviate from this model. Nevertheless, the proposed method remains applicable as long as the probability density function (PDF) of the noise can be analytically described. In particular, the computation of the FIM and the corresponding CRLB can be extended to accommodate non-Gaussian or correlated noise, provided that the underlying distribution is known or can be estimated. In the considered setup, current and voltage are acquired through independent sensors, reducing the likelihood of correlated noise between the two signals. On the other hand, low-frequency effects such as sensor drift introduce a systematic bias that falls outside the scope of the present formulation, which is based on unbiased estimation. However, such issues can be mitigated in practice through proper sensor calibration and drift compensation strategies.

To validate the theoretical approach, it is necessary to compare the quality of the estimated parameters before and after the optimization of the current sample selection. This means to compare:

- The CRLB.
- The estimated parameters $\hat{\boldsymbol{\theta}}$.
- The variance of the estimated parameters.

1) SIMULATION UNDER PARTIAL SHADING CONDITIONS

The synthetic I–V data are generated using the procedure `GenerateIVCurve` from Algorithm 2. Based on these data, the parameter estimates $\hat{\boldsymbol{\theta}}$ are computed 1000 times, which is considered an appropriate number of repetitions to obtain a statistically significant set of values. The mean of the estimated parameters is denoted as $\hat{\boldsymbol{\theta}}_{\mathrm{u}}$. Similarly, the mean of the variances from all estimations, denoted as σ_{u}^2, is taken as the overall variance of the parameter estimation.

The FIM and the CRLB are computed, where the unoptimized CRLB obtained from uniform sampling is denoted as $\mathrm{CRLB}_{\mathrm{u}}$, using the synthetic I–V curve data ($\tilde{\mathbf{v}}_{\mathrm{u}}$ and $\tilde{\mathbf{i}}_{\mathrm{u}}$) and the ground truth parameters $\boldsymbol{\theta}^*$ as inputs. Table 3 presents the

TABLE 3. Results of the estimation using uniform sampling method on a partially shaded simulated module.

String	Parameter	$\mathrm{CRLB}_{\mathrm{u}}$	$\hat{\boldsymbol{\theta}}_{\mathrm{u}}$	σ_{u}^2
String 0	I_{ph} (A)	5.17e-06	9.9992e+00	5.81e-06
	$\log(I_0)$ (-)	3.68e-01	-1.7854e+01	3.80e-01
	n (-)	1.57e-03	1.3604e+00	1.69e-03
	R_{s} (mΩ)	1.14e-04	8.9959e-01	1.52e-04
	R_{sh} (Ω)	4.47e-04	2.0079e+00	5.03e-04
String 1	I_{ph} (A)	5.52e-05	7.0032e+00	6.45e-05
	$\log(I_0)$ (-)	7.49e-01	-1.3647e+01	8.37e-01
	n (-)	7.81e-03	1.5410e+00	8.11e-03
	R_{s} (mΩ)	6.99e-04	5.4944e+00	7.00e-04
	R_{sh} (Ω)	2.53e-02	1.9719e+00	2.78e-02
String 2	I_{ph} (A)	1.04e-03	5.0040e+00	1.07e-03
	$\log(I_0)$ (-)	1.47e+00	-1.2117e+01	2.04e+00
	n (-)	2.62e-02	1.6014e+00	2.97e-02
	R_{s} (mΩ)	3.02e-03	4.8331e+00	3.14e-03
	R_{sh} (Ω)	3.56e-01	2.0425e+00	8.58e-01

numerical results for the unoptimized parameter estimation process.

Figure 6 illustrates the intermediate stages of the optimization process, where the CRLB of each estimated parameter is plotted against the number of iterations. The vertical axis is presented in a logarithmic scale to highlight the magnitude of changes in the variance across iterations. The stopping criterion of the optimization is satisfied when the variation of the logarithm of the determinant of the FIM becomes sufficiently small (on the order of 1e-9) and remains below this level for at least 15 consecutive iterations.

The constrained optimization problem makes sure that the new current sample selection $\tilde{\mathbf{i}}_{\mathrm{opt}}$ falls in the same range as $\tilde{\mathbf{i}}_{\mathrm{init}}$.

Figure 7 illustrates the current sample selection strategy that maximises the determinant of the FIM, as compared to the initial uniformly spaced current selection, in case of PV module under partial shading. Each plot corresponds to one of the three strings of the PV module and shows the optimal selection of current points for that string. Since the strings exhibit different $\mathrm{I_{sc}}$, the total number of valid current samples differs among them. Figure 8 represents the resulting optimised current distribution obtained by combining the contributions of all three strings, capturing the overall information-optimal sampling configuration.

After the optimization, the model parameters are re-estimated using the optimized current sample selection, denoted by $\tilde{\mathbf{i}}_{\mathrm{opt}}$. The newly estimated parameter vector is indicated as $\hat{\boldsymbol{\theta}}_{\mathrm{o}}$, and the corresponding estimated variances are denoted by σ_{o}^2. These variances are observed to closely approach the CRLB, here denoted as $\mathrm{CRLB}_{\mathrm{o}}$.

Table 4 presents the numerical values obtained after the optimization process. By comparing Table 3 with Table 4, a clear improvement of parameter variances appears after optimization.

In the case of the partially shaded simulated module, the application of the optimization procedure led to a consistent reduction in the variances of the estimated parameters. The relative variance improvements are summarized below:

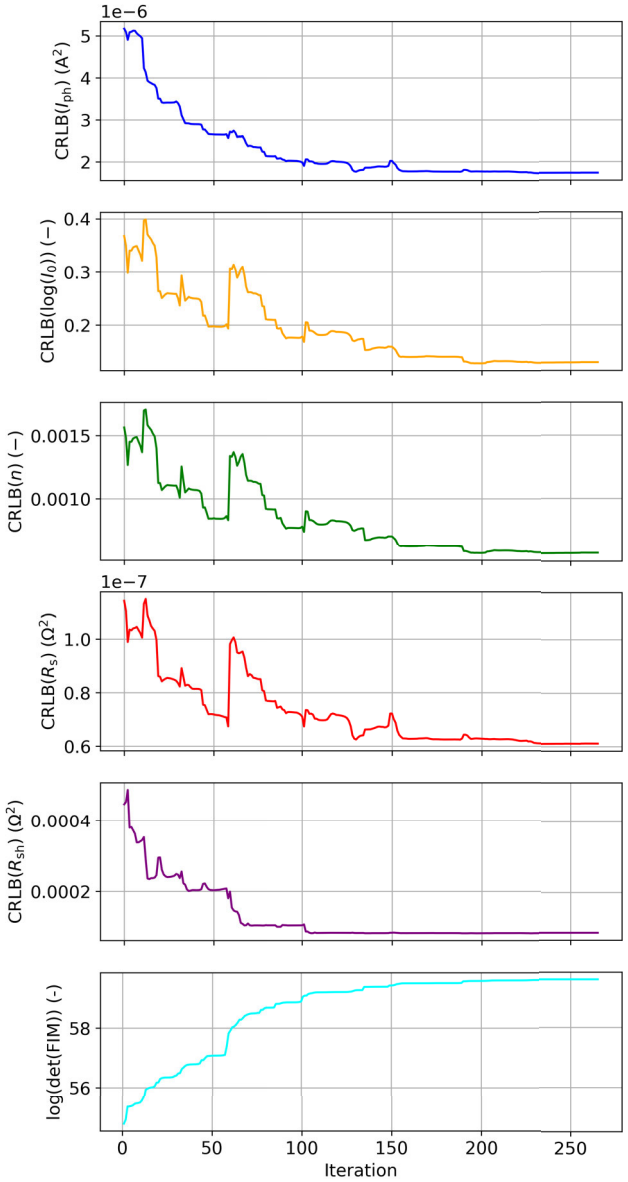

FIGURE 6. Results of the synthetic experiment for the string 0. Each plot shows the CRLB of each parameter as a function of the optimization iterations.

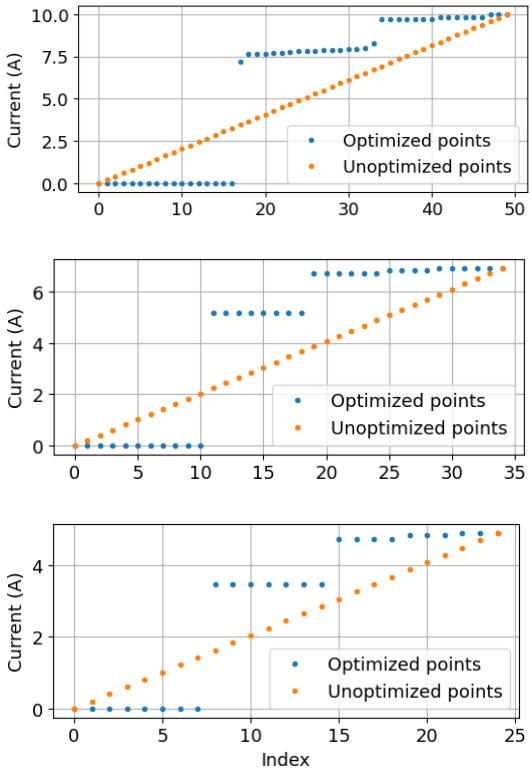

FIGURE 7. Optimized current sample selection compared to the uniform current sample selection for the three strings.

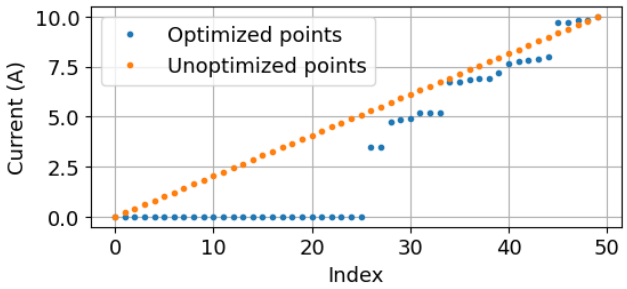

FIGURE 8. The overall optimized current sample selection compared to the uniform current sample selection for $N = 50$ points.

- String 0: the variance was reduced by 26.2% for I_{ph}, 18.4% for $\log(I_0)$, 17.2% for n, 28.9% for R_s, and 55.5% for R_{sh}.
- String 1: the variance was reduced by 80.9% for I_{ph}, 68.3% for $\log(I_0)$, 64.2% for n, 33.0% for R_s, and 42.8% for R_{sh}.
- String 2: the variance was reduced by 90.6% for I_{ph}, 65.1% for $\log(I_0)$, 67.3% for n, 27.4% for R_s, and 98.1% for R_{sh}.

The estimated variances remain close to the corresponding CRLB, indicating that the parameter estimation is statistically efficient in case of partial shading.

These results confirm that the proposed D-optimal sampling approach effectively enhances the accuracy of the parameter estimation process, especially in challenging operating conditions such as partial shading.

2) SIMULATION UNDER UNIFORM IRRADIANCE CONDITIONS

To further validate the effectiveness of the proposed optimization strategy, a second set of simulations was conducted under uniform irradiance conditions. In this configuration, all three strings of the photovoltaic module are assumed to operate under identical environmental and electrical conditions, thereby eliminating any mismatch typically induced by partial shading. Nevertheless, the strings are not identical,

TABLE 4. Results of the estimation using the optimized sampling method on a partially shaded simulated module.

String	Parameter	$\mathrm{CRLB_o}$	$\hat{\theta}_o$	σ_o^2
String 0	I_{ph} (A)	1.77e-06	1.0000e+01	4.29e-06
	$\log(I_0)$ (-)	1.31e-01	-1.7917e+01	3.10e-01
	n (-)	5.73e-04	1.3559e+00	1.40e-03
	R_s (mΩ)	6.26e-05	9.6015e-01	1.08e-04
	R_{sh} (Ω)	8.32e-05	1.9955e+00	2.24e-04
String 1	I_{ph} (A)	6.08e-06	7.0004e+00	1.23e-05
	$\log(I_0)$ (-)	1.26e-01	-1.3173e+01	2.65e-01
	n (-)	1.44e-03	1.5862e+00	2.90e-03
	R_s (mΩ)	2.32e-04	5.2005e+00	4.69e-04
	R_{sh} (Ω)	7.67e-04	2.0048e+00	1.59e-03
String 2	I_{ph} (A)	3.63e-05	5.0030e+00	1.00e-04
	$\log(I_0)$ (-)	2.67e-01	-1.2202e+01	7.71e-01
	n (-)	3.66e-03	1.5798e+00	9.70e-03
	R_s (mΩ)	8.44e-04	5.0631e+00	2.28e-03
	R_{sh} (Ω)	6.91e-03	1.9591e+00	1.64e-02

TABLE 5. Results of the estimation using uniform sampling method on a uniformly-irradiated simulated module.

String	Parameter	$\mathrm{CRLB_u}$	$\hat{\theta}_u$	σ_u^2
String 0	I_{ph} (A)	3.29e-06	9.9997e+00	3.30e-06
	$\log(I_0)$ (-)	2.34e-01	-1.7965e+01	2.35e-01
	n (-)	1.00e-03	1.3534e+00	1.01e-03
	R_s (mΩ)	7.31e-05	1.0139e+00	7.83e-05
	R_{sh} (Ω)	2.56e-04	2.0031e+00	2.87e-04
String 1	I_{ph} (A)	3.31e-06	1.0000e+01	3.41e-06
	$\log(I_0)$ (-)	2.35e-01	-1.7946e+01	2.41e-01
	n (-)	1.00e-03	1.3543e+00	1.04e-03
	R_s (mΩ)	7.31e-05	9.8116e-01	8.09e-05
	R_{sh} (Ω)	2.86e-04	2.0045e+00	2.99e-04
String 2	I_{ph} (A)	3.31e-06	9.9996e+00	3.03e-06
	$\log(I_0)$ (-)	2.35e-01	-1.7908e+01	2.14e-01
	n (-)	9.25e-04	1.3567e+00	9.39e-04
	R_s (mΩ)	7.31e-05	9.5525e-01	8.54e-05
	R_{sh} (Ω)	2.46e-04	2.0007e+00	2.65e-04

so that a small variation of the parameters is expected for the individual strings. Specifically, the ground truth parameters θ^* are set to the same values for all three strings, corresponding to the configuration of string 0 of the partially shaded module seen in Table 1. This setup allows a direct comparison with the partially shaded case and highlights the benefits of current sample optimization even in the absence of irradiance-induced parameter disparity.

As in the previous experiment, synthetic I–V curves are generated using the `GenerateIVCurve` procedure, and the estimation process is repeated 1000 times both before and after the optimization of the current sample selection. The performance is assessed by comparing the CRLB, the estimated parameters $\hat{\theta}$, and the variances of the estimated parameters for each string.

The numerical results for the uniform irradiance scenario, prior to and following the optimization, are summarized in Table 5 and Table 6, respectively.

In the case of the uniformly irradiated simulated PV module, the optimization step led to improvements in the estimation precision, as expressed in terms of relative variance reductions:

TABLE 6. Results of the estimation using the optimized sampling method on a uniformly-irradiated simulated module.

String	Parameter	$\mathrm{CRLB_o}$	$\hat{\theta}_o$	σ_o^2
String 0	I_{ph} (A)	1.05e-06	1.0000e+01	2.67e-06
	$\log(I_0)$ (-)	7.73e-02	-1.8111e+01	2.02e-01
	n (-)	3.38e-04	1.3432e+00	8.57e-04
	R_s (mΩ)	3.08e-05	1.0934e+00	7.33e-05
	R_{sh} (Ω)	5.24e-05	2.0001e+00	1.33e-04
String 1	I_{ph} (A)	1.05e-06	1.0001e+01	2.77e-06
	$\log(I_0)$ (-)	7.73e-02	-1.8095e+01	2.06e-01
	n (-)	3.38e-04	1.3435e+00	8.88e-04
	R_s (mΩ)	3.08e-05	1.0103e+00	7.56e-05
	R_{sh} (Ω)	5.24e-05	1.9893e+00	1.36e-04
String 2	I_{ph} (A)	1.05e-06	1.0000e+01	2.90e-06
	$\log(I_0)$ (-)	7.73e-02	-1.7985e+01	2.12e-01
	n (-)	3.38e-04	1.3512e+00	9.18e-04
	R_s (mΩ)	3.08e-05	9.8322e-01	6.70e-05
	R_{sh} (Ω)	5.24e-05	1.9997e+00	1.46e-04

- String 0: the variance was reduced by 19.1% for I_{ph}, 14.0% for $\log(I_0)$, 15.1% for n, 6.4% for R_s, and 53.7% for R_{sh}.
- String 1: the variance was reduced by 18.8% for I_{ph}, 14.5% for $\log(I_0)$, 14.6% for n, 6.6% for R_s, and 54.5% for R_{sh}.
- String 2: the variance was reduced by 4.3% for I_{ph}, 0.9% for $\log(I_0)$, 2.2% for n, 21.5% for R_s, and 44.9% for R_{sh}.

Finally, as observed under partial shading conditions, the variances of the estimated parameters for the uniformly irradiated PV module closely follow the corresponding CRLB throughout the optimization process. This behaviour confirms the statistical efficiency of the parameter estimation procedure.

3) SENSITIVITY ANALYSIS TO THE INITIAL PARAMETER ERROR

In the simulations presented throughout this work, the FIM and the corresponding CRLB have been computed using the known ground truth parameters. However, in practical applications, the true parameters are not available, and the FIM and CRLB must be evaluated using estimated parameters, which are typically accurate to a certain degree but still subject to uncertainty.

To evaluate the impact of this assumption, a dedicated sensitivity analysis was carried out. Specifically, the effect of variations in the initial parameter values on the resulting CRLB was assessed. The true parameter set was systematically perturbed with relative offsets ranging from 0% to 10%. For each offset level $X \in \{1\%, 2\%, \ldots, 10\%\}$, 1000 random parameter sets were generated by drawing multiplicative perturbations from a uniform distribution within the range $\pm X\%$ for each parameter. For each of these perturbed sets, the FIM and corresponding CRLB were recalculated.

The results are summarized in Figure 9, which presents a series of boxplots, one for each offset level, illustrating the statistical distribution of the CRLB for each parameter across the 1000 repetitions. The results in the figure indicate that the offset becomes significant only when the initial

TABLE 7. Computational performance metrics of the optimization algorithm.

Metric	Value
Execution time (mean)	13.997 s
Execution time (variance)	0.018 s
Memory usage	132.8 MiB
Convergence rate	100%

parameter offset reaches approximately 4–5%. This threshold is relatively high when compared with the accuracy of the estimated parameters shown in Section III-D.

An example is shown in Section III-D1.

4) COMPUTATIONAL PERFORMANCE ANALYSIS

To assess the computational burden of the proposed optimization framework, a systematic benchmarking experiment was conducted. The optimization routine was executed 1000 times on a dedicated workstation equipped with an AMD Ryzen 7 5800X processor and 16 GB of DDR4 RAM, and the key performance metrics were recorded.

In this context, the average execution time per run, the variance of the execution time across trials, the memory usage during execution, and the convergence rate of the algorithm were determined. Table 7 summarizes the results.

The execution time remains consistent across runs, with minimal variance, and the algorithm reliably converges in all cases.

5) SENSITIVITY ANALYSIS TO MEASUREMENT NOISE LEVELS

The estimation framework proposed in this work assumes known levels of measurement noise on both voltage and current signals, derived from typical full-scale range (FSR) specifications. While this assumption is common in the literature, it is important to assess the robustness of the method to variations in these noise levels.

To this end, a dedicated sensitivity analysis was carried out by independently varying the variance of the current and voltage measurements across 90 different levels. For each variance level, the parameter estimation process was repeated, and the empirical variance of the estimated parameters was recorded. This allowed us to quantify how uncertainty in the measurements propagates through the optimization process and impacts the estimation accuracy.

Figure 10 shows the effect of increasing current noise variance on the estimation accuracy of each parameter. Similarly, Figure 11 illustrates the corresponding results for varying voltage noise levels. In both figures, the red marker indicates the noise variances used throughout the rest of the simulation results.

The results confirm that the method remains stable under a wide range of uncertainty levels, showing a smooth increase in parameter variance as a function of measurement noise.

6) STATISTICAL RELIABILITY OF PARAMETER ESTIMATES

To assess the variability and robustness of the estimated parameters under experimental conditions, the statistical distribution of the estimated values across multiple acquisitions is reported. Boxplots are presented to visualize the dispersion and central tendency of the five model parameters for each string, under both uniform and partial irradiance conditions.

Figure 12 shows the results obtained from the uniformly irradiated module. In this case, the parameter estimates exhibit tight clustering and consistent medians across all strings, reflecting the electrical uniformity expected under steady and homogeneous irradiance.

Figure 13 presents the same analysis for the partially shaded module. Greater variability is observed in all five parameters, especially in the photogenerated current I_{ph}, which varies significantly between strings due to the non-uniform irradiance. Similar trends are visible in the ideality factor n and the series resistance R_s, consistent with the altered electrical operating points imposed by shading.

D. EXPERIMENTAL VALIDATION

On-site conditions, the I–V characteristics of a PV module can typically be measured using either an electronic load or a capacitive load. Each technique presents specific advantages and is suitable for different operational contexts. The capacitive method involves charging a capacitor through the PV module, thereby enabling the extraction of the I–V curve in a rapid manner. This approach is particularly well-suited for preliminary diagnostic assessments, as it permits the acquisition of a high number of samples within a short time interval. Moreover, it can be effectively employed under both full irradiance and partial shading conditions. In the present study, the capacitive method was used to preliminarily verify the operational integrity of the PV module under various irradiance conditions.

However, it is important to note that the method proposed in this work for parameter estimation requires the use of an electronic load. Unlike the capacitive method, the electronic load allows for precise control over the operating point by directly imposing the current, a fundamental requirement for the current sample optimization strategy described in Algorithm 1.

The proposed method was experimentally tested on five different commercial PV modules, including:

- A Qcells Q.PEAK DUO M-G11 410 module (monocrystalline silicon),
- An LG370Q1C-V5 module affected by physical defects (back contact),
- A SANYO HIP 230HDE1 module (heterojunction with intrinsic thin layer),
- A JA Solar JAP60S01-280/SC module (polycrystalline silicon),
- A HT-SAAE HT54-18XN-435 module (Tunnel oxide passivated contact (TOPCon)).

Table 8 summarizes the main electrical characteristics at STC for the tested modules.

The scheme of the measurement system is indicated in Figure 14.

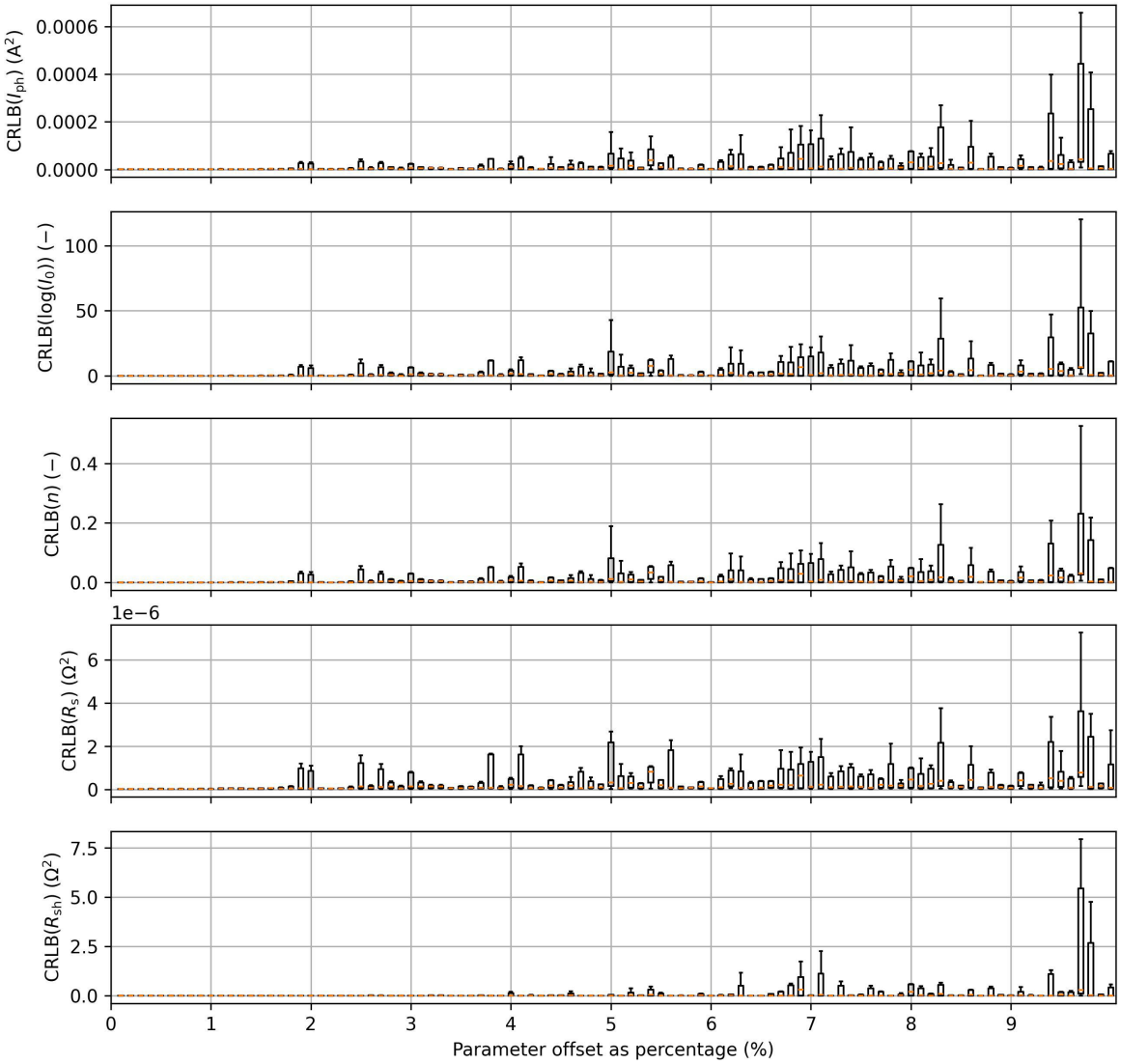

FIGURE 9. CRLB sensitivity analysis under parameter perturbations. Each boxplot shows the distribution of CRLB values obtained from 1000 perturbed parameter sets at a given offset level (0–10%).

TABLE 8. Specifications at STC for the tested PV modules.

Model	P_{mpp} (W)	V_{oc} (V)	V_{mpp} (V)	I_{sc} (A)	I_{mpp} (A)	Tech.	Cells
Q.PEAK DUO M-G11 410	410	37.18	31.22	13.57	12.97	m-Si	108 (half)
LG370Q1C-V5	370	39.9	34.5	11.5	10.73	Back Contact	60
HIP 230HDE1	230	44.6	35.9	5.45	5.1	HIT	72
JAP60S01-280/SC	280	38.65	31.61	9.37	8.86	p-Si	60
HT54-18XN-435	435	38.4	32.0	14.31	13.60	TOPCon	108 (half)

The following devices were used to test the PV module:

- The HH PLA 812 Electronic Load functions both as a DC load and as a measuring device for current and voltage. Table 9 presents the uncertainty of the electronic load. As the electronic load is a precise high-end laboratory instrument, the manufacturer supplies a detailed datasheet, which includes both the reading uncertainty (Δ_{read}) and the uncertainty at FSR (Δ_{FSR}). However, since commercial datasheets typically provide only the FSR uncertainty, this paper assumes a constant variance, equal to the uncertainty calculated at FSR for all readings.
- A Pt100 surface probe to measure the cell temperature of the PV module.
- A reference solar cell to measure the solar irradiance.
- An NI-9219 universal analogue input module for logging temperature and irradiance data.
- An NI-cDAQ-9174 chassis for data acquisition.

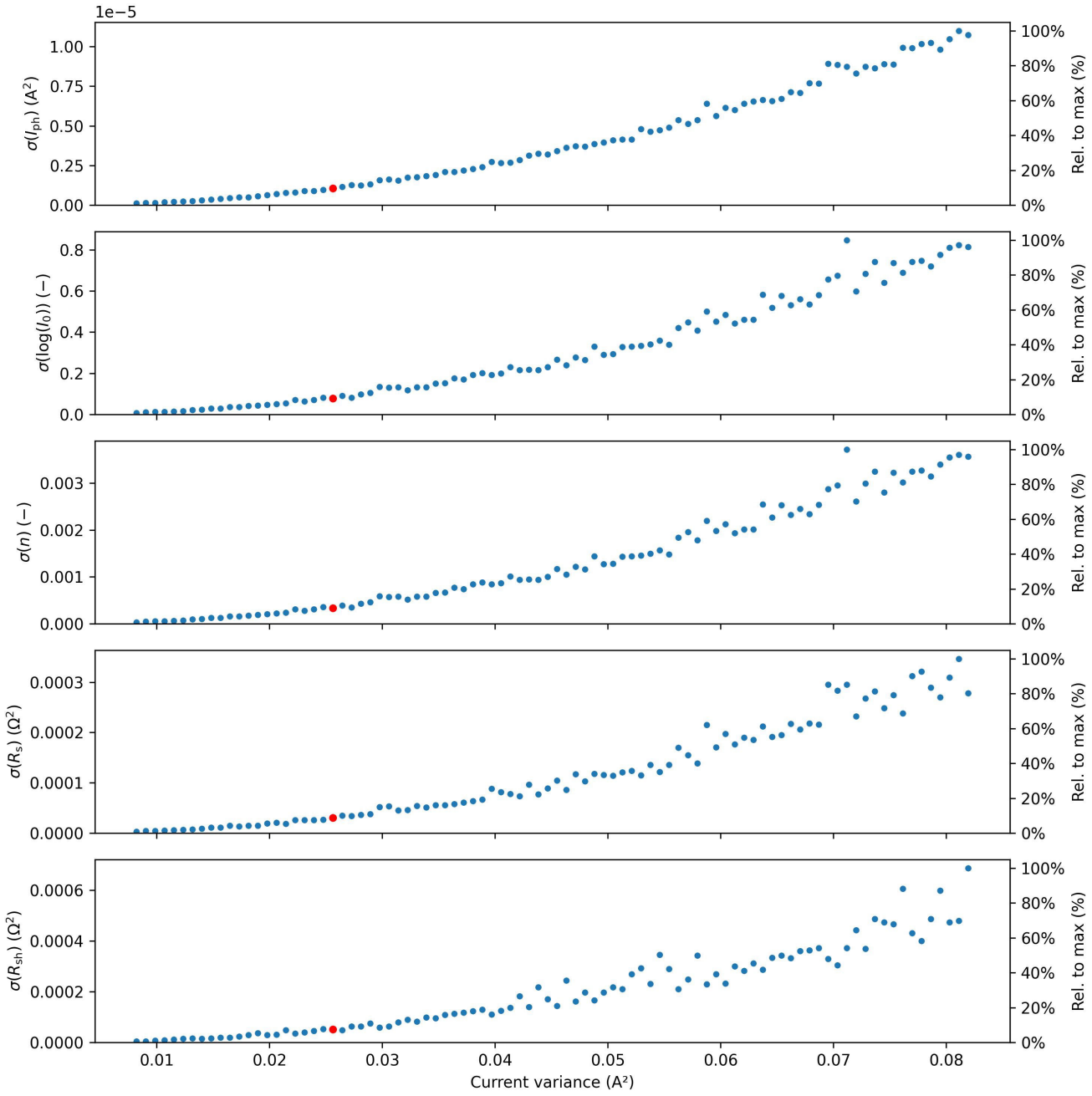

FIGURE 10. Estimation variance of each parameter as a function of current measurement variance. Red markers indicate the value used in other simulations.

- A laptop running LabVIEW software, which controls all components and logs the data.

The proposed method has also been validated on a real PV module operating under natural sunlight. The procedure followed is identical to that described in Algorithm 1, the key difference being that the noisy I–V measurements were obtained from actual experimental data. It is important to note that, since the PV module is a real system, the true parameter values are not known. Therefore, the estimated parameters are used to compute the FIM and the CRLB. The number of points considered is 50 and the reason for using this number is explained in Section IV.

1) QCELLS Q.PEAK DUO M-G11 410 MODULE

Environmental Conditions:

- Partial shading: $T_c = 40.22°\text{C}$, $G = 986.3\ \text{W/m}^2$
- Uniform irradiance: $T_c = 41.37°C\text{C}$, $G = 1001.6\ \text{W/m}^2$

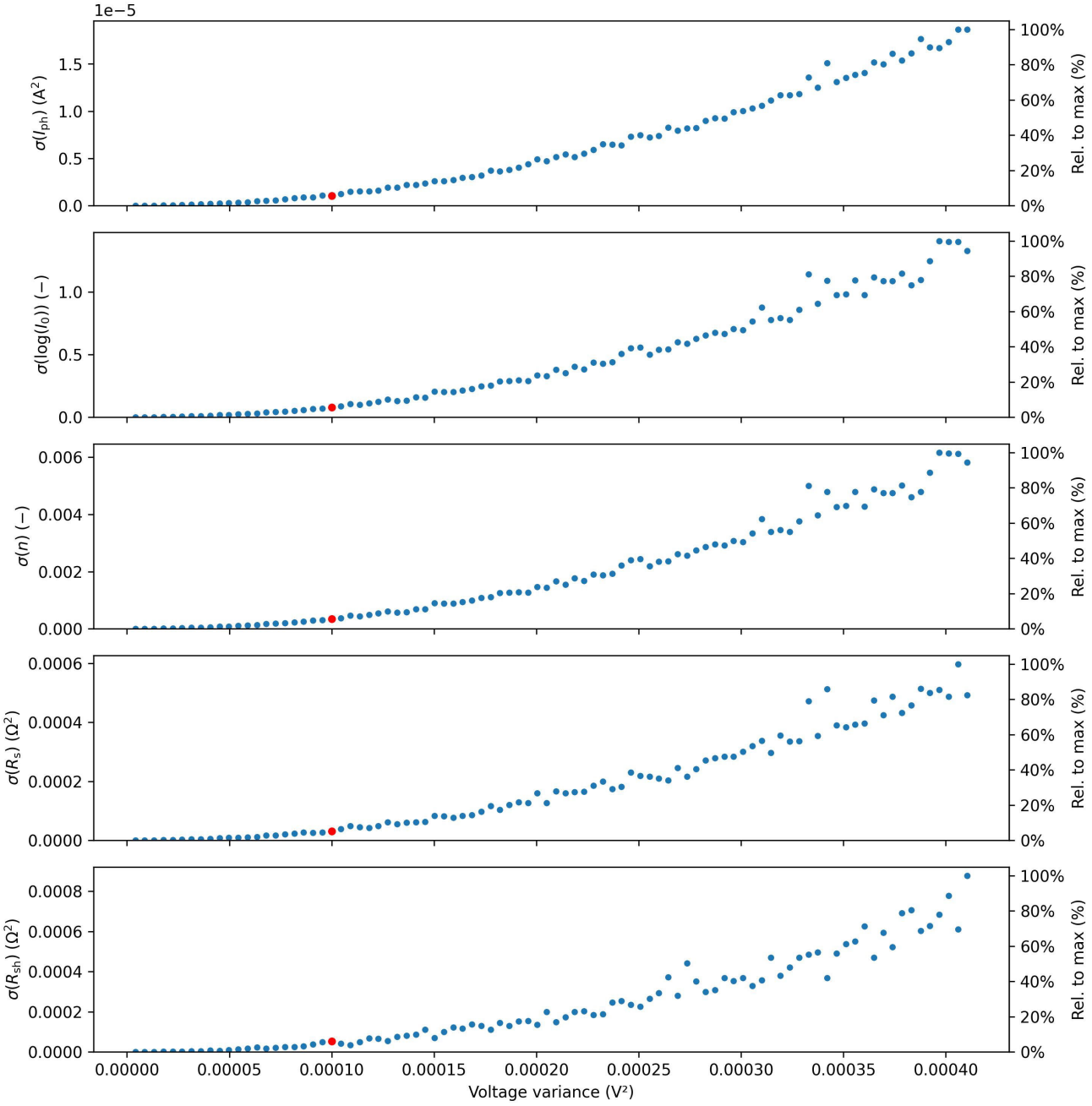

FIGURE 11. Estimation variance of each parameter as a function of voltage measurement variance. Red markers indicate the value used in other simulations.

TABLE 9. Electrical characteristics of the measurement system.

	V	I
$\Delta_{\text{read}}(3\sigma)$	$\pm$ 0.1%	$\pm$ 0.2%
$\Delta_{\text{FSR}}(3\sigma)$	$\pm$ 0.05%	$\pm$ 0.05%
FSR	100 (V)	18 (A)
σ^2	2.5 (mV^2)	0.225 (mA^2)

The specific shading pattern used for the Q.PEAK DUO M-G11 410 module is shown in Figure 15. Two vertical regions of the panel were masked to simulate realistic shading scenarios across different substrings. This physical setup was used to replicate the intended irradiance profile during the test campaign.

Figure 16 shows the I–V characteristics gathered during the experimental validation under partially shaded conditions. The blue dots show the preliminary measurements obtained with the capacitive load technique. The orange marks show the I–V curve points measured by the electronic load by uniformly covering the entire current range. The green marks show the optimally selected current samples. Table 10 shows

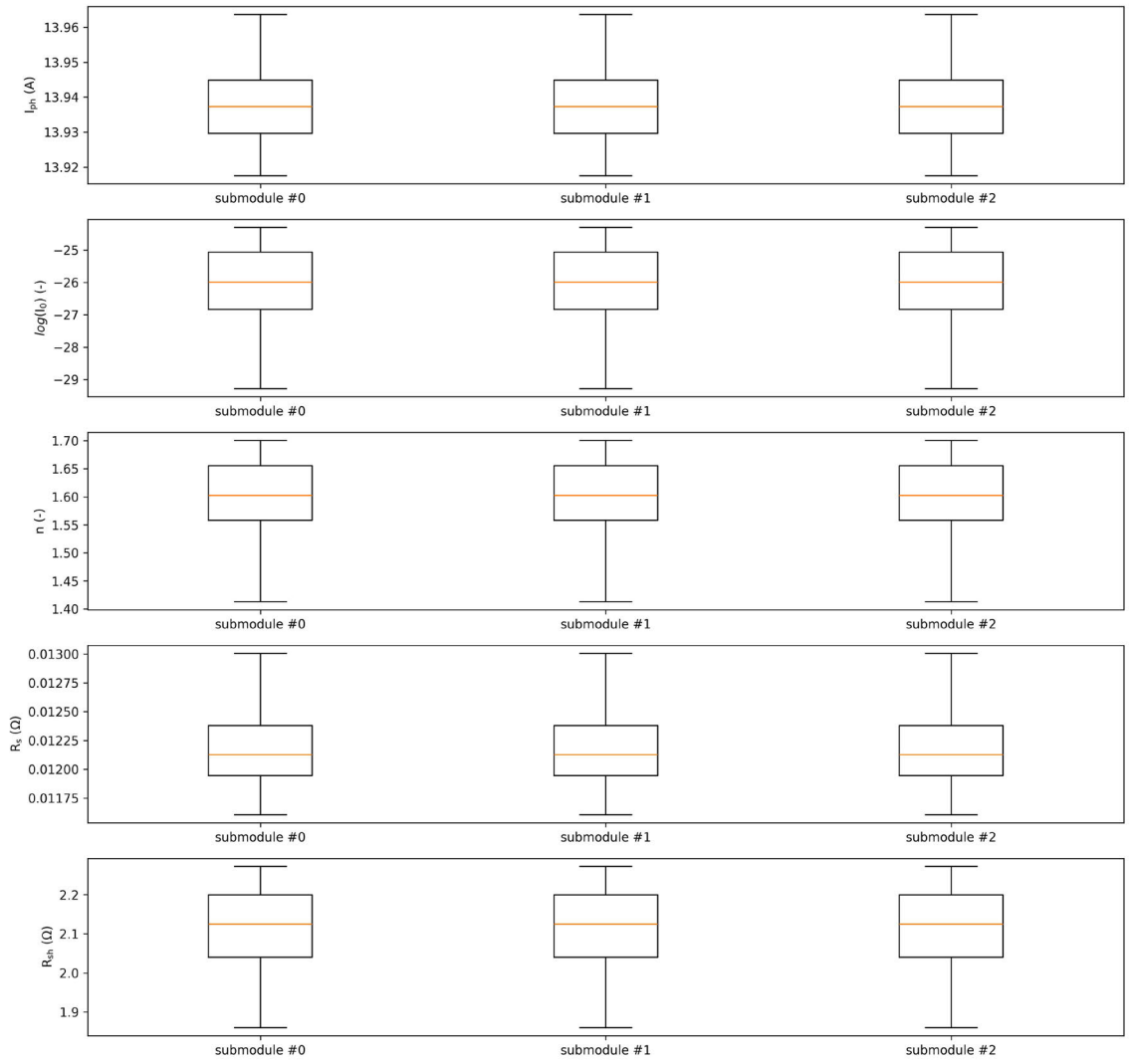

FIGURE 12. Boxplots of estimated parameters for each strings of the uniformly irradiated QCells module.

TABLE 10. Current and voltage points as percentages of I_{sc} and V_{oc} under partial shading using the optimized sampling method. The MPP is highlighted.

Index	Current (% I_{sc})	Voltage (% V_{oc})	Power (% P_{mpp})	
1–25	0.00	100.00	0.00	
26–27	34.70–34.72	92.76–92.75	45.11–45.82	
28–30	47.16–48.98	84.60–74.13	100.00	MPP
31–33	51.80–51.83	64.02–64.01	85.01–84.73	
34–38	67.20–69.39	55.84–40.01	58.62–55.93	
39	72.22	34.63	36.55	
40–44	76.84–80.05	34.22–33.88	23.81–23.06	
45–50	100.00	0.00	0.00	

the selected current and voltage sample points as a percentage of I_{sc} and V_{oc}, respectively. The table also highlights the MPP, providing manufacturers and PV plants operators a tool to better track the MPP of PV modules under partial shading.

Table 11 and Table 12 report the estimated model parameters using the uniform sampling method and the D-optimal current sampling method respectively. The optimization procedure was applied to improve the accuracy of the parameter identification process in the presence of non-uniform irradiance, where the model identifiability is intrinsically more challenging.

The reduction of the variance and its close correlation to the CRLB, reinforce the value of the proposed D-optimal sampling method in conditions where irradiance is spatially non-uniform and model identifiability is intrinsically more challenging.

Figure 17 shows the I–V characteristics gathered during the experimental validation under fully irradiated conditions. The blue dots correspond to the preliminary I–V curve points measured using the capacitive load technique. The orange marks represent the current samples obtained by imposing

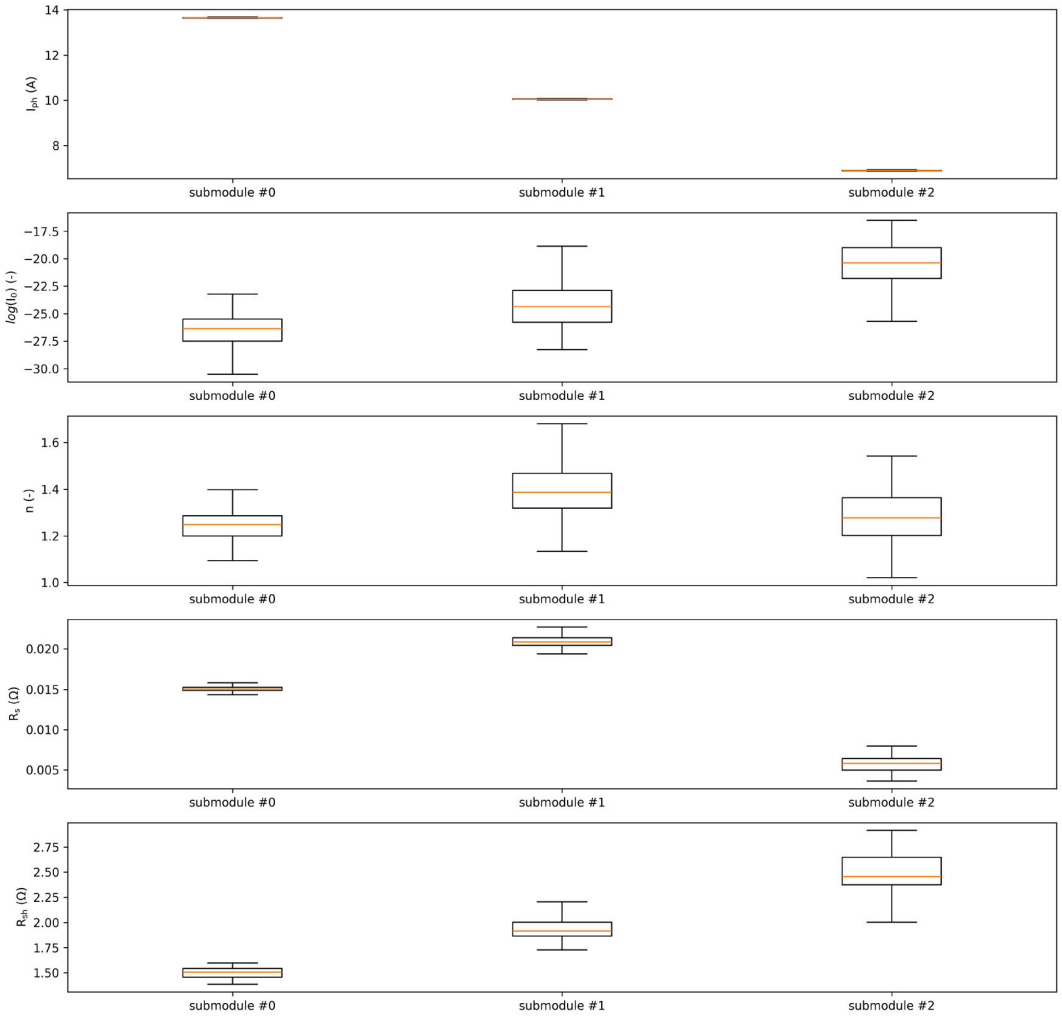

FIGURE 13. Boxplots of estimated parameters for each strings of the partially shaded QCells module.

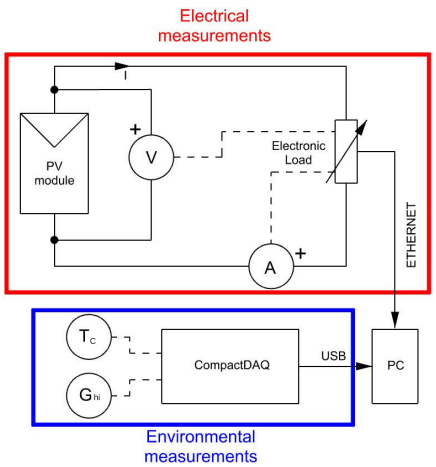

FIGURE 14. Scheme of the measurement system.

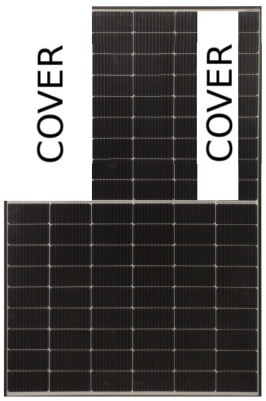

FIGURE 15. Partial shading configuration applied to the Q.PEAK DUO M-G11 410 module during the experimental validation.

a uniformly spaced current sampling strategy through an electronic load. The green marks highlight the points selected by the D-optimal current sampling method. Table 13 shows the selected current and voltage sample points as a percentage of I_{sc} and V_{oc} respectively. The table also highlights the MPP,

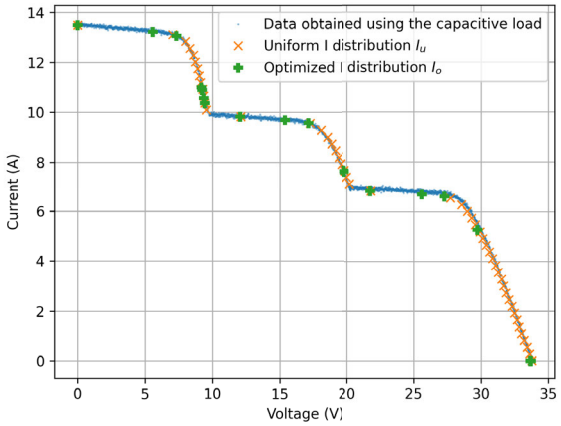

FIGURE 16. Measured *I–V* curves under partial shading conditions (Q.PEAK DUO M-G11 410 Module).

TABLE 11. Results of the estimation using the uniform sampling method on the partially shaded module.

String	Parameter	$CRLB_u$	$\hat{\theta}_u$	σ_u^2
String 0	I_{ph} (A)	5.23e-06	1.3643e+01	5.30e-06
	$\log(I_0)$ (-)	1.83e-01	-2.5894e+01	1.98e-01
	n (-)	3.85e-04	1.2690e+00	3.87e-04
	R_s (mΩ)	1.22e-05	1.4907e+01	1.24e-05
	R_{sh} (Ω)	1.53e-04	1.5178e+00	1.58e-04
String 1	I_{ph} (A)	4.48e-05	9.9307e+00	8.97e-04
	$\log(I_0)$ (-)	3.61e-01	-1.6598e+01	1.46e+00
	n (-)	9.64e-04	1.9487e+00	1.52e-02
	R_s (mΩ)	4.41e-05	1.7435e+01	4.72e-05
	R_{sh} (Ω)	2.78e-03	3.7637e+00	1.19e+00
String 2	I_{ph} (A)	1.82e-05	6.8540e+00	1.52e-04
	$\log(I_0)$ (-)	6.99e-01	-1.3668e+01	2.13e+00
	n (-)	2.27e-03	1.8199e+00	2.80e-02
	R_s (mΩ)	1.78e-05	1.2372e+00	1.51e-03
	R_{sh} (Ω)	1.58e-02	5.0944e+00	5.29e+00

TABLE 12. Results of the estimation using the optimized sampling method on the partially shaded module.

String	Parameter	$CRLB_o$	$\hat{\theta}_o$	σ_o^2
String 0	I_{ph} (A)	6.28e-07	1.3643e+01	1.50e-06
	$\log(I_0)$ (-)	3.43e-02	-2.5967e+01	8.23e-02
	n (-)	6.67e-05	1.2655e+00	1.59e-04
	R_s (mΩ)	4.23e-06	1.4933e+01	1.01e-05
	R_{sh} (Ω)	5.63e-06	1.5192e+00	1.35e-05
String 1	I_{ph} (A)	1.11e-06	1.0043e+01	2.98e-06
	$\log(I_0)$ (-)	4.53e-02	-2.4385e+01	1.23e-01
	n (-)	1.23e-04	1.3858e+00	3.31e-04
	R_s (mΩ)	1.18e-05	2.0915e+01	3.18e-05
	R_{sh} (Ω)	3.22e-05	1.9252e+00	8.71e-05
String 2	I_{ph} (A)	4.50e-07	6.8922e+00	1.69e-06
	$\log(I_0)$ (-)	4.87e-02	-2.0301e+01	1.83e-01
	n (-)	1.60e-04	1.2831e+00	6.04e-04
	R_s (mΩ)	3.72e-05	5.7674e+00	1.41e-04
	R_{sh} (Ω)	4.18e-05	2.4586e+00	1.59e-04

providing manufacturers and PV plants operators a tool to better track the MPP of PV modules under partial shading.

Table 14 and Table 15 summarize the results of the parameter estimation procedure using the uniform sampling strategy and the optimized sampling strategy, respectively, in the case of a uniformly irradiated module. For the module

TABLE 13. Current and voltage points as percentages of I_{sc} and V_{oc} under uniform irradiation using the optimized sampling method. The MPP is highlighted.

Index	Current (% I_{sc})	Voltage (% V_{oc})	Power (% P_{mpp})	
1–15	0.00	100.00	0.00	
16	68.62	92.97	85.40	
17	70.98	92.51	89.20	
18–20	73.85–74.20	91.81–91.89	94.50–95.10	
21	76.20	91.33	97.80	
22	80.44	90.14	99.20	
23	82.67	89.39	99.80	
24	84.26	88.78	100.00	MPP
25–31	96.64–96.99	74.19–71.72	92.50–91.40	
32–35	98.08–98.10	53.07–52.49	64.20–63.80	
36–50	100.00	0.00	0.00	

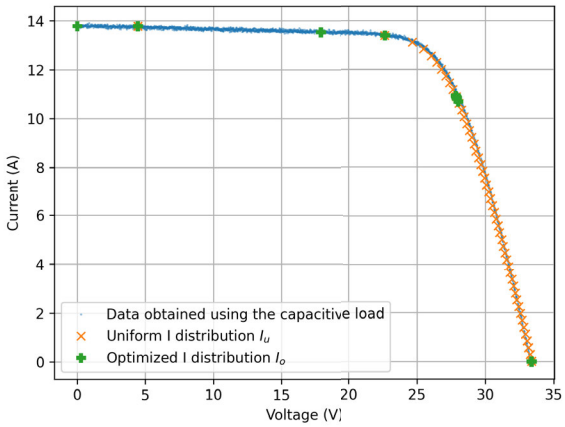

FIGURE 17. Measured *I–V* curves under fully irradiated conditions(Q.PEAK DUO M-G11 410 Module).

under uniform irradiance and using the optimized sampling, the CRLB values for string 0 reported in Table 15 are 6.23e-07 A^2 for I_{ph}, 4.02e-02 for $\log(I_0)$, 1.23e-04 for n, 7.00e-12 for $R_s\Omega^2$, and 1.30e-05 for $R_{sh}\Omega^2$. Compared with the largest values observed across the offset sweep performed in Section III-C5 and shown in Figure 9 (up to ≈ 6e-04 A^2, ≈ 1e+02, ≈ 4e-01, ≈ 1e-06 Ω^2, and ≈ 8e+00 Ω^2, respectively), these values are lower by roughly three to five orders of magnitude.

The consistency of the results obtained for the PV module under uniform irradiance conditions highlights the robustness of the D-optimal sampling strategy. The observed correlation between the parameter variances and their respective CRLB, throughout the optimization process, further confirms the statistical efficiency of the estimation procedure on real, uniformly irradiated PV modules.

2) LG370Q1C-V5 MODULE (DEFECTIVE)

Environmental Conditions:

- Partial shading: $T_c = 47.16°C$, $G = 782.9\ W/m^2$
- Uniform irradiance: $T_c = 46.76°C$, $G = 786.9\ W/m^2$

The LG370Q1C-V5 module tested in this study exhibits manufacturing defects that were visually confirmed by

TABLE 14. Results of the estimation using the uniform sampling method on the QCells module under uniform irradiation.

String	Parameter	$CRLB_u$	$\hat{\theta}_u$	σ_u^2
String 0	I_{ph} (A)	1.28e-05	1.3819e+01	2.04e-03
	$\log(I_0)$ (-)	3.11e-01	-9.6950e+00	4.55e+00
	n (-)	9.41e-04	1.6625e+00	3.87e-03
	R_s (mΩ)	2.56e-05	1.7141e+00	5.63e-03
	R_{sh} (Ω)	1.19e-03	2.0815e+00	2.87e-03
String 1	I_{ph} (A)	1.28e-05	1.3818e+01	2.03e-03
	$\log(I_0)$ (-)	3.11e-01	-9.7150e+00	4.52e+00
	n (-)	9.41e-04	1.6582e+00	3.82e-03
	R_s (mΩ)	2.56e-05	1.8172e+00	5.57e-03
	R_{sh} (Ω)	1.19e-03	2.0756e+00	2.83e-03
String 2	I_{ph} (A)	1.28e-05	1.3819e+01	2.18e-03
	$\log(I_0)$ (-)	3.11e-01	-9.5514e+00	4.70e+00
	n (-)	9.41e-04	1.7047e+00	4.19e-03
	R_s (mΩ)	2.56e-05	1.5420e+00	6.03e-03
	R_{sh} (Ω)	1.19e-03	2.1406e+00	3.28e-03

TABLE 15. Results of the estimation using the optimized sampling method on the uniformly irradiated QCells module.

String	Parameter	$CRLB_o$	$\hat{\theta}_o$	σ_o^2
String 0	I_{ph} (A)	6.23e-07	1.3938e+01	2.25e-04
	$\log(I_0)$ (-)	4.02e-02	-2.6205e+01	1.46e-01
	n (-)	1.23e-04	1.5913e+00	4.42e-04
	R_s (mΩ)	7.00e-06	1.2218e+01	2.51e-04
	R_{sh} (Ω)	1.30e-05	2.0954e+00	4.64e-05
String 1	I_{ph} (A)	6.23e-07	1.3938e+01	2.34e-06
	$\log(I_0)$ (-)	4.02e-02	-2.6156e+01	1.52e-01
	n (-)	1.23e-04	1.5943e+00	4.60e-04
	R_s (mΩ)	7.00e-06	1.2210e+01	2.61e-04
	R_{sh} (Ω)	1.30e-05	2.0945e+00	4.80e-05
String 2	I_{ph} (A)	6.23e-07	1.3938e+01	2.16e-06
	$\log(I_0)$ (-)	4.02e-02	-2.6147e+01	1.40e-01
	n (-)	1.23e-04	1.5945e+00	4.27e-04
	R_s (mΩ)	7.00e-06	1.2189e+01	2.42e-04
	R_{sh} (Ω)	1.30e-05	2.0969e+00	4.48e-05

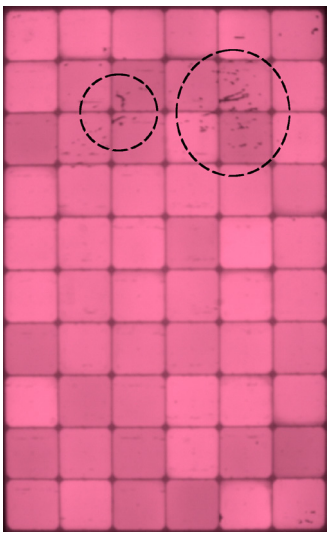

FIGURE 18. Electroluminescence image of the LG370Q1C-V5 module highlighting cell-level defects.

electroluminescence imaging. Figure 18 shows the electroluminescence image of the module, highlighting regions with inactive or degraded cells.

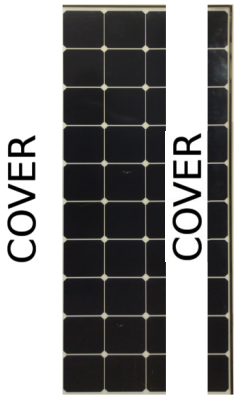

FIGURE 19. Photograph of the LG370Q1C-V5 module with applied shading pattern used during partial shading tests.

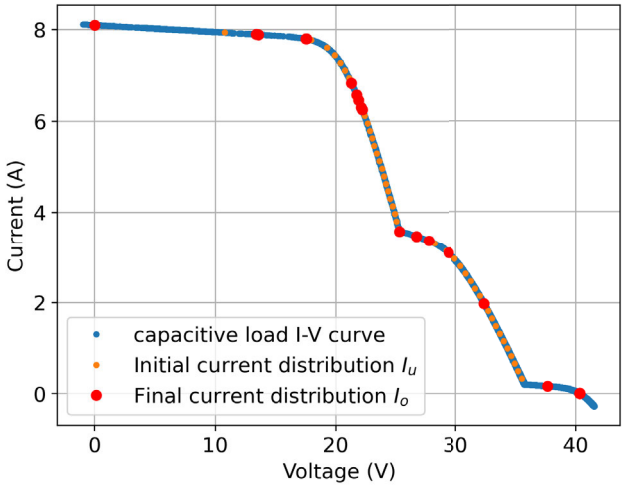

FIGURE 20. Measured *I–V* curves under partial shading conditions (LG370Q1C-V5).

During the experimental validation, partial shading was applied to the module by intentionally covering two of its three strings: one string was fully shaded, and another was shaded approximately halfway along its length. This configuration is depicted in Figure 19, which shows the module layout and the position of the artificial shading.

The figure shows the actual image of the LG370Q1C-V5 module during the test, with the labelled "COVER" regions clearly indicating the fully and partially shaded areas. This visual support complements the earlier schematic by offering a practical view of how the masking was applied to the physical module surface.

Figure 20 shows the *I–V* characteristics gathered during the experimental validation under partially shaded conditions. The blue dots correspond to the preliminary measurements acquired using the capacitive load method. The orange marks indicate the uniformly distributed current samples measured using the electronic load, and the green marks represent the D-optimal current samples selected by the proposed algorithm.

TABLE 16. Current and voltage points as percentages of I_{sc} and V_{oc} under partial shading using the optimized sampling method (LG370Q1C-V5). The MPP is highlighted.

Index	Current (% I_{sc})	Voltage (% V_{oc})	Power (% P_{mpp})	
1	0.00	100.00	0.00	
2	33.66	97.42	73.69	
3	43.39	96.27	93.87	
4	43.56	96.22	94.19	
5	52.78	84.31	100.00	MPP
6	53.83	81.13	98.13	
7	54.27	79.67	97.16	
8	54.82	77.80	95.83	
9	54.99	77.18	95.38	
10	62.68	44.10	62.11	
11	66.13	42.85	63.68	
12	66.13	42.85	63.68	
13	68.76	41.55	64.20	
14	72.82	38.24	62.58	
15	80.27	24.43	44.07	
16	93.35	2.04	4.28	
17-50	100.00	0.00	0.00	

TABLE 17. Results of the estimation using the uniform sampling method on the partially shaded LG370Q1C-V5 module.

String	Parameter	$CRLB_u$	$\hat{\theta}_u$	σ_u^2
String 0	I_{ph} (A)	2.97e-07	8.2007	2.77e-05
	$\log(I_0)$ (-)	4.20e-02	-30.1785	1.55e-01
	n (-)	1.10e-04	1.6550	4.02e-04
	R_s (mΩ)	1.35e-05	41.048	2.91e-05
	R_{sh} (Ω)	4.91e-05	3.2094	3.84e-03
String 1	I_{ph} (A)	2.97e-07	3.8067	6.72e-04
	$\log(I_0)$ (-)	4.20e-02	-10.2872	4.44e-01
	n (-)	1.10e-04	1.1955	4.71e-03
	R_s (mΩ)	1.35e-05	30.875	9.44e-04
	R_{sh} (Ω)	4.91e-05	0.5246	1.33e-03
String 2	I_{ph} (A)	2.97e-07	0.2012	1.90e-04
	$\log(I_0)$ (-)	4.20e-02	-9.7692	2.27e+01
	n (-)	1.10e-04	1.0357	2.31e-01
	R_s (mΩ)	1.35e-05	6.8135	2.80e-01
	R_{sh} (Ω)	4.91e-05	2.5665	5.60e+00

TABLE 18. Results of the estimation using the optimized sampling method on the partially shaded LG370Q1C-V5 module.

String	Parameter	$CRLB_o$	$\hat{\theta}_o$	σ_o^2
String 0	I_{ph} (A)	7.04e-08	8.1055	2.65e-03
	$\log(I_0)$ (-)	1.49e-02	-25.5249	2.74e+00
	n (-)	3.99e-05	1.9331	1.34e-02
	R_s (mΩ)	7.12e-06	38.915	5.75e-04
	R_{sh} (Ω)	4.55e-06	4.5669	1.15e+00
String 1	I_{ph} (A)	2.08e-07	3.8055	4.36e-04
	$\log(I_0)$ (-)	2.78e-02	-10.3690	2.96e-01
	n (-)	6.99e-05	1.1941	2.73e-03
	R_s (mΩ)	8.12e-06	29.115	5.95e-04
	R_{sh} (Ω)	2.91e-05	0.6363	8.88e-04
String 2	I_{ph} (A)	2.38e-07	0.9861	1.51e-04
	$\log(I_0)$ (-)	2.63e-02	-8.5220	1.37e+01
	n (-)	7.24e-05	1.0912	1.67e-01
	R_s (mΩ)	1.01e-05	6.2951	1.95e-01
	R_{sh} (Ω)	3.29e-05	2.6083	4.04e+00

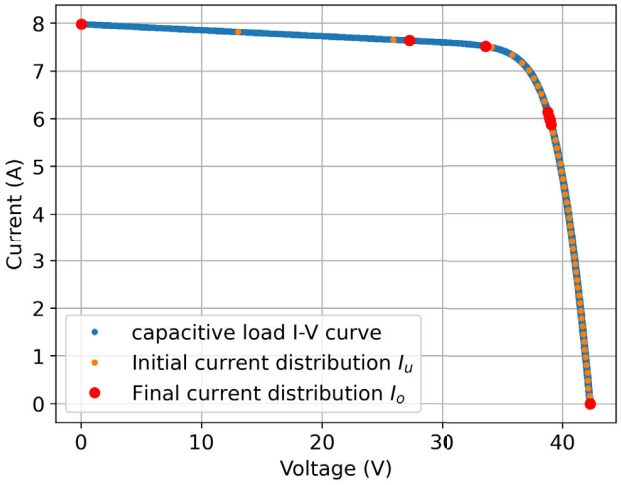

FIGURE 21. Measured *I–V* curves under uniform irradiance (LG370Q1C-V5).

Table 16 reports the selected current and voltage sample points as a percentage of I_{sc} and V_{oc}, respectively. The Maximum Power Point (MPP) is highlighted in the table, providing a useful reference for PV plant operators to enhance MPP tracking performance under mismatched conditions.

Table 17 and Table 18 report the results of the parameter estimation performed using the uniform and optimized sampling methods, respectively. As in the previous test case, the optimization was applied to improve parameter identifiability in a context where spatially variable irradiance and module defects can significantly impair estimation accuracy.

To complement the partial shading analysis, the LG370Q1C-V5 module was also tested under uniform irradiance conditions. This experiment allows for evaluating the parameter estimation procedure in the presence of manufacturing defects but without irradiance mismatch.

Figure 21 shows the measured *I–V* curve under uniform irradiance. The blue dots represent the preliminary curve obtained using the capacitive load method. The orange marks correspond to a uniformly spaced current sampling pattern imposed via electronic load, while the green marks indicate the D-optimal sample points selected by the proposed algorithm.

Table 19 summarizes the selected current and voltage sample points, expressed as percentages of I_{sc} and V_{oc}, respectively. The Maximum Power Point (MPP) is also highlighted to facilitate performance tracking under standard conditions.

The results of the parameter estimation procedure under uniform irradiance are reported in Table 20 and Table 21, corresponding to the uniform and optimized sampling methods, respectively.

3) SANYO HIP 230HDE1 MODULE (HIT TECHNOLOGY)

Environmental Conditions:

- Partial shading: $T_c = 62.02°C$, $G = 967.8\ W/m^2$
- Uniform irradiance: $T_c = 57.52°C$, $G = 974.1\ W/m^2$

The SANYO HIP 230HDE1 module, based on Heterojunction with Intrinsic Thin layer (HIT) technology, was

TABLE 19. Current and voltage points as percentages of I_{sc} and V_{oc} under uniform irradiation using the optimized sampling method (LG370Q1C-V5). The MPP is highlighted.

Index	Current (% I_{sc})	Voltage (% V_{oc})	Power (% P_{mpp})	
1-5	0.00	100.00	0.00	
6	64.44	95.70	82.25	
7	64.46	95.70	82.26	
8	64.46	95.69	82.27	
9	64.47	95.69	82.28	
10	64.47	95.69	82.28	
11	64.48	95.69	82.30	
12	64.52	95.69	82.35	
13	79.62	94.15	99.98	
14	79.63	94.15	99.98	
15	79.63	94.15	99.99	
16	79.63	94.15	99.99	
17	79.63	94.15	99.99	
18	79.63	94.15	99.99	
19	79.63	94.15	99.99	
20	79.64	94.15	99.99	
21	79.64	94.15	100.00	MPP
22	91.71	76.87	94.02	
23	91.98	75.66	92.81	
24	92.05	75.34	92.48	
25	92.08	75.18	92.33	
26	92.15	74.82	91.96	
27	92.16	74.80	91.93	
28	92.16	74.80	91.93	
29	92.16	74.77	91.90	
30	92.17	74.75	91.88	
31	92.19	74.66	91.79	
32	92.19	74.63	91.76	
33	92.23	74.44	91.57	
34	92.43	73.44	90.53	
35-50	100.00	0.00	0.00	

TABLE 20. Results of the estimation using the uniform sampling method on the LG370Q1C-V5 module under uniform irradiation.

String	Parameter	CRLBo	$\hat{\theta}$u	σ_u^2
String 0	I_{ph} (A)	1.03e-06	7.9999	1.15e-06
	$\log(I_0)$ (-)	1.49e-01	-28.2961	1.72e-01
	n (-)	3.38e-04	1.4357	3.76e-04
	R_s (mΩ)	4.37e-05	5.0661	4.87e-05
	R_{sh} (Ω)	3.70e-05	2.1972	4.12e-05
String 1	I_{ph} (A)	1.03e-06	8.0003	1.01e-06
	$\log(I_0)$ (-)	1.49e-01	-27.8825	1.46e-01
	n (-)	3.38e-04	1.4556	3.36e-04
	R_s (mΩ)	4.37e-05	4.9692	4.33e-05
	R_{sh} (Ω)	3.70e-05	2.2025	3.67e-05
String 2	I_{ph} (A)	1.03e-06	7.9997	1.19e-06
	$\log(I_0)$ (-)	1.49e-01	-28.2035	1.78e-01
	n (-)	3.38e-04	1.4405	3.92e-04
	R_s (mΩ)	4.37e-05	5.0955	5.07e-05
	R_{sh} (Ω)	3.70e-05	2.2025	4.30e-05

experimentally tested under both uniform irradiance and partial shading conditions.

In the partial shading test, the sub-module configuration of the device plays a critical role. In particular, one of the three series-connected strings is composed of a reduced number of cells compared to the others. This structural characteristic leads to a different electrical behaviour, which is clearly reflected in the I–V curve acquired under shading.

Figure 22 displays the I–V measurements gathered under partial shading using both the capacitive load and electronic load methods. The blue dots represent the full-span curve

TABLE 21. Results of the estimation using the optimized sampling method on the LG370Q1C-V5 module under uniform irradiation.

String	Parameter	CRLBo	$\hat{\theta}$o	σ_o^2
String 0	I_{ph} (A)	6.89e-07	8.0013	8.36e-07
	$\log(I_0)$ (-)	1.08e-01	-27.9514	1.10e-01
	n (-)	2.58e-04	1.4527	2.79e-04
	R_s (mΩ)	3.13e-05	5.0182	3.62e-05
	R_{sh} (Ω)	2.82e-05	2.2051	3.04e-05
String 1	I_{ph} (A)	7.68e-07	8.0022	8.44e-07
	$\log(I_0)$ (-)	1.23e-01	-27.9872	1.05e-01
	n (-)	2.71e-04	1.4562	2.15e-04
	R_s (mΩ)	2.96e-05	4.9423	3.10e-05
	R_{sh} (Ω)	2.56e-05	2.1984	3.43e-05
String 2	I_{ph} (A)	9.92e-07	7.9990	9.73e-07
	$\log(I_0)$ (-)	1.44e-01	-28.1005	1.07e-01
	n (-)	2.45e-04	1.4483	2.23e-04
	R_s (mΩ)	3.50e-05	5.0736	4.00e-05
	R_{sh} (Ω)	3.15e-05	2.2044	3.38e-05

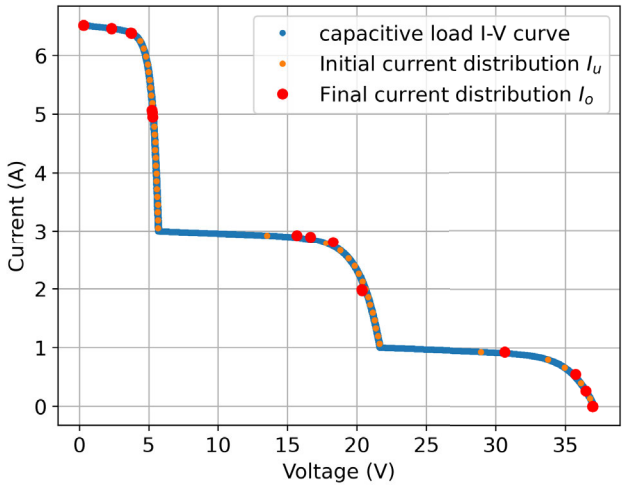

FIGURE 22. Measured I–V curves under partial shading conditions (SANYO HIP 230HDE1).

measured with the capacitive load, the orange marks indicate uniformly spaced current samples, and the green marks denote the optimized sampling points computed by the D-optimal algorithm.

Table 22 reports the current and voltage sample points selected through optimization, expressed as percentages of I_{sc} and V_{oc}. The Maximum Power Point (MPP) is also highlighted.

Figure 23 shows the physical implementation of the partial shading test applied to the SANYO HIP 230HDE1 module. The image clearly shows the regions that were masked to simulate shading, allowing controlled application of non-uniform irradiance across the sub-modules. This visual evidence complements the electrical characterization by confirming the precise geometry of the test.

Table 23 and Table 24 present the parameter estimates obtained using the uniform and optimized sampling strategies, respectively. The variance reduction confirms the effectiveness of the D-optimal method even in the presence of structural asymmetries in the module architecture.

TABLE 22. Current and voltage points as percentages of I_{sc} and V_{oc} under partial shading using the optimized sampling method (SANYO HIP 230HDE1). The MPP is highlighted.

Index	Current (% I_{sc})	Voltage (% V_{oc})	Power (% P_{mpp})	
1-4	0.00	100.00	0.00	
5	6.26	99.13	29.10	
6	6.30	99.13	29.31	
7	10.05	97.99	46.19	
8	10.18	97.90	46.74	
9	14.17	77.71	51.66	
10	14.20	77.17	51.41	
11	14.27	75.97	50.84	
12	42.40	44.89	89.27	
13	45.05	44.56	94.12	
14	49.47	43.11	100.00	MPP
15	55.09	30.50	78.80	
16	55.14	30.24	78.19	
17	82.95	14.28	55.56	
18	96.67	8.42	38.17	
19	98.69	4.08	18.88	
20-50	100.00	0.00	0.00	

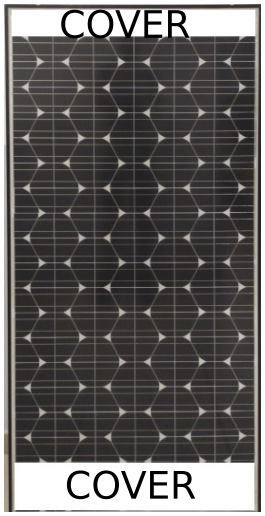

FIGURE 23. Physical layout of the SANYO HIP 230HDE1 module under partial shading conditions.

TABLE 23. Results of the estimation using the uniform sampling method on the partially shaded SANYO HIP 230HDE1 module.

String	Parameter	CRLBu	$\hat{\theta}$u	σ_u^2
String 0	I_{ph} (A)	8.40e-07	6.5171	8.54e-05
	$\log(I_0)$ (-)	7.82e-02	-8.5231	3.73e+00
	n (-)	6.27e-04	1.7170	9.68e-02
	R_s (mΩ)	6.51e-05	0.1543	7.23e-03
	R_{sh} (Ω)	1.10e-02	5.0465	2.72e+01
String 1	I_{ph} (A)	8.40e-07	2.9510	3.39e-03
	$\log(I_0)$ (-)	7.82e-02	-10.8982	2.60e+00
	n (-)	6.27e-04	1.3813	3.31e-02
	R_s (mΩ)	6.51e-05	0.6512	6.09e-03
	R_{sh} (Ω)	1.10e-02	8.9671	5.31e+02
String 2	I_{ph} (A)	8.40e-07	1.0209	6.00e-03
	$\log(I_0)$ (-)	7.82e-02	-13.5422	2.94e+01
	n (-)	6.27e-04	1.1346	1.86e-01
	R_s (mΩ)	6.51e-05	1.3684	2.54e-01
	R_{sh} (Ω)	1.10e-02	3.2658	3.84e+02

Figure 24 shows the results of the same module under uniform irradiance conditions. The uniform and optimized

TABLE 24. Results of the estimation using the optimized sampling method on the partially shaded SANYO HIP 230HDE1 module.

String	Parameter	CRLBo	$\hat{\theta}$o	σ_o^2
String 0	I_{ph} (A)	2.87e-07	6.5231	2.21e-05
	$\log(I_0)$ (-)	2.51e-02	-11.7665	8.48e-01
	n (-)	2.14e-04	1.2789	2.66e-02
	R_s (mΩ)	2.26e-02	0.140	2.75
	R_{sh} (Ω)	4.84e-03	2.9194	5.68e+00
String 1	I_{ph} (A)	1.84e-07	3.0291	1.02e-03
	$\log(I_0)$ (-)	3.34e-02	-11.5922	9.34e-01
	n (-)	2.32e-04	1.2673	1.76e-02
	R_s (mΩ)	1.91e-02	0.120	2.19
	R_{sh} (Ω)	3.73e-03	2.9231	8.23e+00
String 2	I_{ph} (A)	4.42e-07	1.0386	1.94e-03
	$\log(I_0)$ (-)	1.75e-02	-12.2965	1.02e+00
	n (-)	1.63e-04	1.2738	3.74e-02
	R_s (mΩ)	2.79e-02	0.100	58.1
	R_{sh} (Ω)	5.47e-03	2.9202	1.44e+01

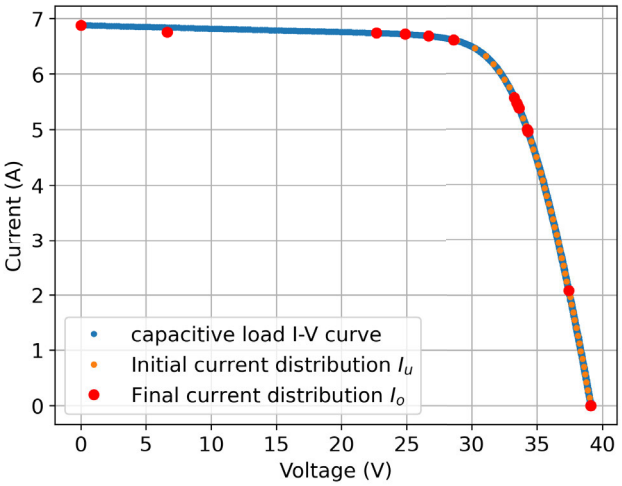

FIGURE 24. Measured *I–V* curves under uniform irradiance conditions (SANYO HIP 230HDE1).

sampling patterns are highlighted over the full I–V curve. The corresponding sampling percentages and MPP identification are reported in Table 25.

Table 26 and Table 27 summarize the outcomes of the parameter estimation under uniform irradiance conditions, using the uniform sampling strategy and the D-optimal sampling strategy, respectively.

4) JA SOLAR MODULE (POLYCRYSTALLINE–VOLTAGE SAMPLING)

Environmental Conditions:

- Uniform irradiance: $T_c = 44.85°C$, $G = 991.0\ W/m^2$

To investigate the feasibility of voltage-based sampling, a polycrystalline silicon PV module from JA Solar was experimentally tested under uniform irradiance conditions. In this configuration, the voltage was imposed directly using an electronic load, while the resulting current was recorded. The D-optimal sampling procedure was adapted to operate

TABLE 25. Current and voltage points as percentages of I_{sc} and V_{oc} under uniform irradiation using the optimized sampling method (SANYO HIP 230HDE1). The MPP is highlighted.

Index	Current (% I_{sc})	Voltage (% V_{oc})	Power (% P_{mpp})	
1	0.00	100.00	0.00	
2	16.92	98.23	23.63	
3	16.94	98.23	23.66	
4	57.98	97.95	80.73	
5	57.98	97.95	80.73	
6	57.98	97.95	80.73	
7	63.59	97.66	88.29	
8	63.59	97.66	88.29	
9	63.60	97.66	88.29	
10	63.60	97.66	88.29	
11	63.60	97.66	88.29	
12	63.60	97.66	88.30	
13	68.17	97.23	94.22	
14	68.18	97.22	94.23	
15	73.16	96.14	99.99	
16	73.16	96.14	99.99	
17	73.16	96.14	99.99	
18	73.16	96.14	99.99	
19	73.16	96.14	99.99	
20	73.17	96.14	100.00	MPP
21	85.04	80.90	97.80	
22	85.47	79.63	96.75	
23	85.60	79.24	96.42	
24	85.82	78.56	95.84	
25	85.94	78.16	95.50	
26	87.54	72.57	90.31	
27	87.64	72.16	89.91	
28	87.65	72.15	89.90	
29	87.65	72.12	89.86	
30	87.66	72.10	89.85	
31	87.67	72.07	89.81	
32	87.68	72.03	89.78	
33	95.65	30.19	41.05	
34-50	100.00	0.00	0.00	

TABLE 26. Results of the estimation using the uniform sampling method on the SANYO HIP 230HDE1 module under uniform irradiance.

String	Parameter	CRLBu	$\hat{\theta}$u	σ_u^2
String 0	I_{ph} (A)	2.98e-07	6.8582	3.86e-02
	$\log(I_0)$ (-)	8.84e-02	-20.6462	4.98e+00
	n (-)	2.40e-04	1.3115	4.60e-02
	R_s (mΩ)	3.54e-05	8.259	2.19e-03
	R_{sh} (Ω)	1.79e-04	4.7805	7.92e+01
String 1	I_{ph} (A)	2.98e-07	6.8573	3.78e-02
	$\log(I_0)$ (-)	8.84e-02	-20.6808	5.04e+00
	n (-)	2.40e-04	1.3071	4.61e-02
	R_s (mΩ)	3.54e-05	8.196	2.22e-03
	R_{sh} (Ω)	1.79e-04	4.7683	7.69e+01
String 2	I_{ph} (A)	2.98e-07	6.8582	3.83e-02
	$\log(I_0)$ (-)	8.84e-02	-20.6372	4.90e+00
	n (-)	2.40e-04	1.3121	4.53e-02
	R_s (mΩ)	3.54e-05	8.232	2.16e-03
	R_{sh} (Ω)	1.79e-04	4.7822	7.86e+01

in the voltage domain rather than current, and was executed using the same information-theoretic framework.

Figure 25 shows the results of this experiment. The blue line represents the full I–V curve measured using a capacitive load. The orange dots correspond to the initial uniform voltage distribution, while the red dots indicate the final optimized voltage sample locations derived from the D-optimal strategy.

TABLE 27. Results of the estimation using the optimized sampling method on the SANYO HIP 230HDE1 module under uniform irradiance.

String	Parameter	CRLBo	$\hat{\theta}$o	σ_o^2
String 0	I_{ph} (A)	1.19e-07	6.8912	1.27e-02
	$\log(I_0)$ (-)	3.54e-02	-21.9451	1.59e+00
	n (-)	9.61e-05	1.2664	1.55e-02
	R_s (mΩ)	1.15e-05	10.951	0.85e-03
	R_{sh} (Ω)	5.42e-05	3.4262	2.87e+01
String 1	I_{ph} (A)	1.29e-07	6.9023	1.38e-02
	$\log(I_0)$ (-)	3.70e-02	-21.9763	1.63e+00
	n (-)	1.01e-04	1.2637	1.66e-02
	R_s (mΩ)	1.21e-05	10.895	0.91e-03
	R_{sh} (Ω)	5.76e-05	3.4131	2.94e+01
String 2	I_{ph} (A)	1.24e-07	6.8956	1.35e-02
	$\log(I_0)$ (-)	3.62e-02	-21.9824	1.61e+00
	n (-)	9.98e-05	1.2641	1.58e-02
	R_s (mΩ)	1.18e-05	10.912	0.88e-03
	R_{sh} (Ω)	5.60e-05	3.4227	2.91e+01

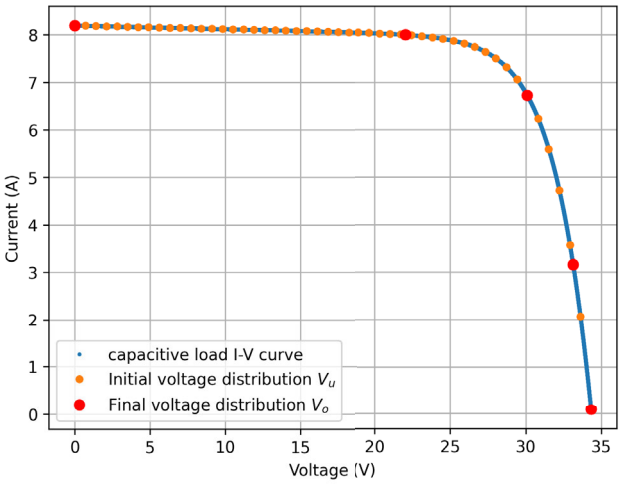

FIGURE 25. Measured I–V curve and optimized voltage sampling points under uniform irradiance (JA Solar polycrystalline module).

As clearly shown, the optimized samples are concentrated in areas of the I–V curve associated with high parameter sensitivity, namely, the short-circuit region and the transition zone following the elbow. This aligns with the results observed in current-based sampling for uniformly irradiated modules.

The present test on the JA Solar module demonstrates that the D-optimal design methodology can be effectively adapted to such setups, thus supporting its broader applicability.

Table 28 reports the selected voltage and corresponding current samples, expressed as percentages of the open-circuit voltage V_{oc} and short-circuit current I_{sc}, respectively. The MPP region is also highlighted for reference.

This experimental validation confirms the applicability of the D-optimal design methodology in the voltage domain. For uniformly irradiated PV modules, where sub-module mismatch is absent and all cells contribute equally to the electrical output, voltage sampling can serve as an effective and practical alternative to current sampling.

TABLE 28. Voltage and current points as percentages of V_{oc} and I_{sc} under uniform irradiation using the optimized sampling method (JA Solar). The MPP is highlighted.

Index	Current (% I_{sc})	Voltage (% V_{oc})	Power (% P_{mpp})	
1-15	0.00	100.00	0.00	
16	64.15	97.60	87.04	
17	64.16	97.60	87.05	
18	64.19	97.60	87.08	
19	64.20	97.60	87.10	
20	64.21	97.60	87.11	
21	64.21	97.60	87.11	
22	64.22	97.60	87.12	
23	87.67	82.06	100.00	MPP
24	87.67	82.05	99.99	
25	87.68	82.04	99.98	
26	87.68	82.04	99.98	
27	87.68	82.03	99.97	
28	87.68	82.03	99.97	
29	87.69	82.01	99.96	
30	87.69	82.00	99.95	
31	87.70	81.99	99.94	
32	96.53	38.53	51.70	
33	96.53	38.53	51.69	
34	96.53	38.52	51.68	
35	96.53	38.52	51.68	
36	96.53	38.52	51.68	
37	96.53	38.51	51.68	
38	96.53	38.51	51.68	
39-50	100.00	1.13	1.57	

TABLE 29. Estimation results for the JA Solar polycrystalline module under uniform irradiance using voltage-based sampling.

Sampling	Parameter	CRLB	$\hat{\theta}$	σ^2
Uniform	I_{ph} (A)	3.12e-05	8.2162e+00	3.11e-05
	$\log(I_0)$ (-)	4.30e-02	-1.3984e+01	4.26e-02
	n (-)	5.31e-04	1.8102e+00	5.30e-04
	R_s (mΩ)	1.70e-05	9.8237e-01	1.70e-05
	R_{sh} (Ω)	2.49e-02	3.0633e+00	2.71e-02
Optimized	I_{ph} (A)	2.56e-05	8.2016e+00	2.55e-05
	$\log(I_0)$ (-)	3.81e-02	-1.4034e+01	3.77e-02
	n (-)	4.47e-04	1.8050e+00	4.46e-04
	R_s (mΩ)	1.39e-05	9.9641e-01	1.39e-05
	R_{sh} (Ω)	1.91e-02	3.0312e+00	2.08e-02

Moreover, this flexibility enables broader compatibility with PV test systems where voltage control is easier or more stable than current control, thus expanding the real-world applicability of the proposed technique.

5) HT54-18XN-435 MODULE (MONOCRYSTALLINE HALF-CUT CELLS)

Environmental Conditions:

- Partial shading: $T_c = 48.23°C$, $G = 919.6\ W/m^2$
- Uniform irradiance: $T_c = 47.63°C$, $G = 924.7\ W/m^2$

Figure 26 and Figure 27 show the measured I–V characteristics under partial shading and uniform irradiance conditions, respectively, for the HT54-18XN-435 module based on monocrystalline half-cut cell technology. In both operating scenarios, the D-optimal sampling strategy identifies the most informative current values along the curve, ensuring high-accuracy parameter estimation with a reduced number of points. The physical configuration used to apply shading

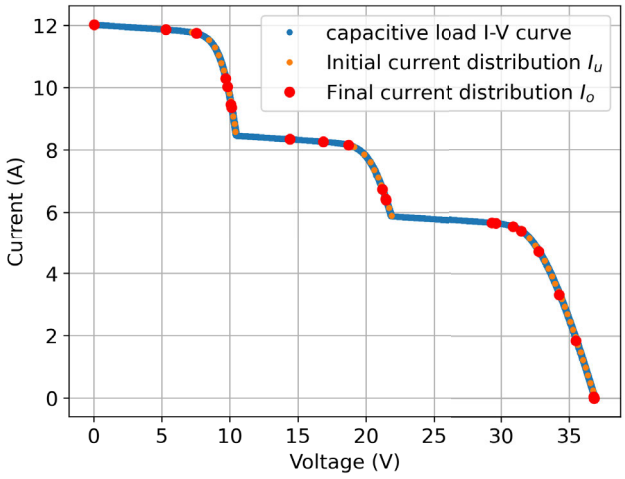

FIGURE 26. Measured I–V curves under partial shading conditions (HT54-18XN-435 module).

TABLE 30. Current and voltage points as percentages of I_{sc} and V_{oc} under partial shading using the optimized sampling method (HT54-18XN-435 module). The MPP is highlighted.

Index	Current (% I_{sc})	Voltage (% V_{oc})	Power (% P_{mpp})	
1	0.00	100.00	0.00	
2	14.38	98.66	36.89	
3	14.38	98.66	36.90	
4	20.43	97.69	51.89	
5	20.45	97.69	51.95	
6	20.51	97.67	52.09	
7	26.32	85.61	58.59	
8	26.68	83.44	57.90	
9	27.38	78.63	55.99	
10	27.49	77.81	55.62	
11	39.09	69.38	70.53	
12	39.09	69.38	70.53	
13	45.78	68.75	81.83	
14	45.78	68.75	81.84	
15	50.82	67.82	89.63	
16	57.54	56.00	83.79	
17	58.19	53.47	80.90	
18	58.27	53.16	80.55	
19	79.58	46.93	97.12	
20	80.39	46.82	97.88	
21	83.85	45.86	100.00	MPP
22	85.48	44.72	99.39	
23	88.93	39.29	90.87	
24	93.04	27.65	66.91	
25	96.37	15.34	38.46	
26	99.92	0.32	0.85	
27	99.99	0.01	0.02	
28-50	100.00	0.00	0.00	

on the HT54-18XN-435 module is the one already shown in Figure 3, where the masked areas are clearly visible.

IV. DETERMINATION OF NUMBER OF SELECTED POINTS FOR I–V CURVE SWEEP

The previous results refer to a fixed number of current sample points. To maximize the benefit of the proposed current sampling selection method, it is crucial to determine an appropriate number of voltage and current measurements that balance the trade-off between computational efficiency and estimation accuracy.

TABLE 31. Results of the estimation using the uniform sampling method on the partially shaded HT54-18XN-435 module.

String	Parameter	CRLBu	$\hat{\theta}$u	σ_u^2
String 0	I_{ph} (A)	1.15e-06	12.0781	1.15e-06
	$\log(I_0)$ (-)	6.12e-02	-18.9970	6.02e-02
	n (-)	3.66e-04	1.7057	3.69e-04
	R_s (mΩ)	1.441	12.13	1.443
	R_{sh} (Ω)	4.89e-04	2.6170	5.20e-04
String 1	I_{ph} (A)	1.01e-04	8.4980	1.05e-04
	$\log(I_0)$ (-)	2.63e-01	-18.9792	2.60e-01
	n (-)	1.64e-03	1.7071	1.68e-03
	R_s (mΩ)	8.095	12.08	8.194
	R_{sh} (Ω)	2.32e-02	2.6346	2.69e-02
String 2	I_{ph} (A)	1.25e-02	5.9141	1.24e-02
	$\log(I_0)$ (-)	1.68e+00	-19.1600	1.66e+00
	n (-)	1.09e-02	1.6964	1.11e-02
	R_s (mΩ)	6.2155	12.12	6.3072
	R_{sh} (Ω)	1.37e+00	2.9135	1.01e+01

TABLE 32. Results of the estimation using the optimized sampling method on the partially shaded HT54-18XN-435 module.

String	Parameter	CRLBo	$\hat{\theta}$o	σ_o^2
String 0	I_{ph} (A)	1.82e-07	12.0789	4.26e-07
	$\log(I_0)$ (-)	1.04e-02	-19.0498	2.42e-02
	n (-)	6.31e-05	1.7012	1.49e-04
	R_s (mΩ)	4.4858	12.16	1.0547
	R_{sh} (Ω)	1.84e-05	2.6031	4.36e-05
String 1	I_{ph} (A)	1.16e-06	8.4993	3.60e-06
	$\log(I_0)$ (-)	2.61e-02	-19.0102	8.02e-02
	n (-)	1.66e-04	1.7045	5.15e-04
	R_s (mΩ)	2.211	12.06	6.857
	R_{sh} (Ω)	1.41e-04	2.6055	4.38e-04
String 2	I_{ph} (A)	3.32e-04	5.9144	6.13e-04
	$\log(I_0)$ (-)	1.64e-01	-19.3788	3.17e-01
	n (-)	1.07e-03	1.6761	1.96e-03
	R_s (mΩ)	1.4652	12.40	2.7342
	R_{sh} (Ω)	3.54e-02	2.4736	5.62e-02

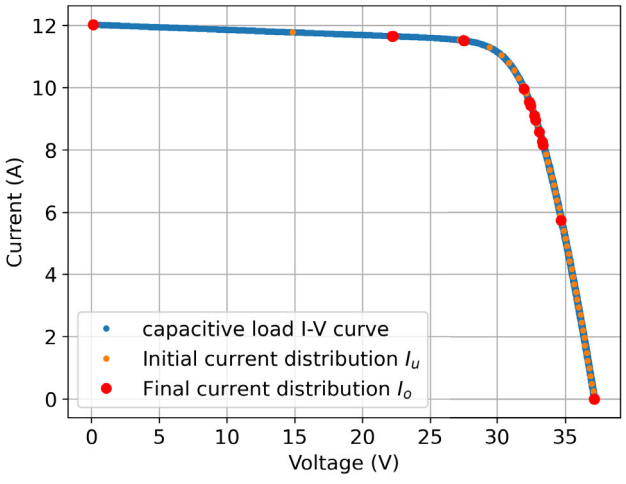

FIGURE 27. Measured *I–V* curves under uniform irradiance conditions (HT54-18XN-435 module).

It is important to note that the algorithm is fully independent of the number of sampling points selected. Its purpose is not to decide how many points should be measured, but rather to redistribute a user-defined number of points

TABLE 33. Current and voltage points as percentages of I_{sc} and V_{oc} under uniform irradiance using the optimized sampling method (HT54-18XN-435 module). The MPP is highlighted.

Index	Current (% I_{sc})	Voltage (% V_{oc})	Power (% P_{mpp})	
1-7	0.00	100.00	0.00	
8	59.75	96.93	81.22	
9	59.78	96.93	81.26	
10	59.79	96.93	81.27	
11	59.82	96.93	81.31	
12	59.83	96.93	81.33	
13	59.87	96.93	81.37	
14	59.91	96.93	81.43	
15	60.02	96.92	81.58	
16	74.22	95.76	99.67	
17	74.27	95.75	99.73	
18	74.30	95.75	99.77	
19	74.31	95.74	99.78	
20	74.31	95.74	99.78	
21	74.32	95.74	99.79	
22	74.33	95.75	99.80	
23	86.14	82.78	100.00	MPP
24	87.19	79.36	97.04	
25	87.29	79.01	96.72	
26	87.46	78.38	96.14	
27	88.18	75.64	93.53	
28	88.45	74.52	92.44	
29	89.19	71.31	89.19	
30	89.74	68.75	86.51	
31	89.92	67.86	85.57	
32	93.48	47.70	62.53	
33-50	100.00	0.00	0.00	

TABLE 34. Results of the estimation using the uniform sampling method on the uniformly irradiated HT54-18XN-435 module.

String	Parameter	CRLBu	$\hat{\theta}$u	σ_u^2
String 0	I_{ph} (A)	2.33e-06	12.0809	2.74e-06
	$\log(I_0)$ (-)	2.20e-01	-29.4074	2.68e-01
	n (-)	7.73e-04	1.8794	9.04e-04
	R_s (mΩ)	4.237e-01	1.229	4.940e-01
	R_{sh} (Ω)	1.42e-04	2.5860	1.62e-04
String 1	I_{ph} (A)	2.33e-06	12.0779	2.38e-06
	$\log(I_0)$ (-)	2.20e-01	-28.8261	2.18e-01
	n (-)	7.73e-04	1.9140	7.96e-04
	R_s (mΩ)	4.237e-01	1.207	4.371e-01
	R_{sh} (Ω)	1.42e-04	2.6058	1.48e-04
String 2	I_{ph} (A)	2.33e-06	12.0803	2.45e-06
	$\log(I_0)$ (-)	2.20e-01	-29.2212	2.34e-01
	n (-)	7.73e-04	1.8906	8.11e-04
	R_s (mΩ)	4.237e-01	1.222	4.447e-01
	R_{sh} (Ω)	1.42e-04	2.5948	1.49e-04

along the *I–V* curve in a way that minimizes the determinant of the CRLB. In doing so, the algorithm prioritizes regions of the curve where the information gain is the highest, thereby improving the accuracy of the parameter estimation.

The information content of the measurements is quantified through the volume of the confidence ellipsoid derived from the FIM, which is used as the optimization objective. As shown in Figure 28, the elbow criterion is applied to this volume, illustrating how the amount of information increases with the number of samples, both before and after optimization.

Based on this analysis, a total of 50 sampling points is selected, corresponding to the threshold beyond which further

TABLE 35. Results of the estimation using the optimized sampling method on the uniformly irradiated HT54-18XN-435 module.

String	Parameter	CRLBo	$\hat{\theta}$o	σ_o^2
String 0	I_{ph} (A)	9.68e-07	12.0795	1.43e-06
	$\log(I_0)$ (-)	8.93e-02	-29.1062	1.72e-01
	n (-)	3.36e-04	1.8976	5.04e-04
	R_s (mΩ)	2.1284	12.18	3.2058
	R_{sh} (Ω)	5.32e-05	2.5979	7.63e-05
String 1	I_{ph} (A)	7.55e-07	12.0793	1.65e-06
	$\log(I_0)$ (-)	7.41e-02	-29.0755	1.68e-01
	n (-)	2.76e-04	1.8964	4.85e-04
	R_s (mΩ)	2.0865	12.13	3.1074
	R_{sh} (Ω)	5.15e-05	2.5974	6.73e-05
String 2	I_{ph} (A)	1.01e-06	12.0791	1.81e-06
	$\log(I_0)$ (-)	6.64e-02	-29.1608	1.65e-01
	n (-)	2.94e-04	1.8962	4.77e-04
	R_s (mΩ)	1.8494	12.17	2.9360
	R_{sh} (Ω)	4.87e-05	2.5975	6.34e-05

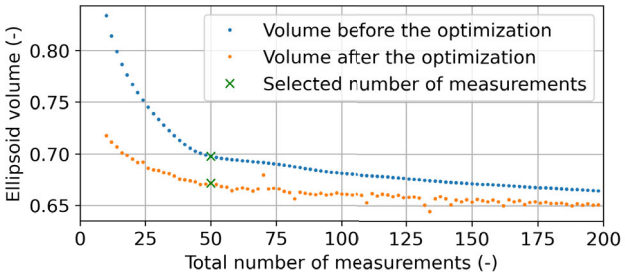

FIGURE 28. Volume of the confidence ellipsoid associated with the FIM before and after optimization.

increases yield only marginal improvements in estimation performance.

It is worth noting that the optimization procedure for 50 points requires approximately 14 seconds of computation time on a standard personal computer equipped with an AMD Ryzen 7 5800X processor and 16 GB of DDR4 RAM As such, while the method is well-suited for offline analysis and characterization tasks, it is not yet compatible with applications under strict real-time constraints, such as high-speed Maximum Power Point (MPP) tracking updates.

V. CONCLUDING REMARKS

In this paper, a rigorous method for optimizing the selection of current sample points for I–V curve measurements of PV modules has been presented. The proposed approach leverages the Fisher Information Matrix to quantify the accuracy of parameter estimates and reduces the overall variance through optimized measurements. The validity of the method has been confirmed through both numerical simulations and real-world experiments. The proposed method demonstrates that reliable estimation of the equivalent circuit parameters of a PV module can be achieved from a measured I–V characteristic using a relatively small number of sample points.

The experimental validation conducted on five commercial PV modules, characterized by different technologies and architectures, confirmed substantial improvements in parameter identifiability under both fully irradiated and partially shaded conditions. One of the tested modules presented visible defects, further demonstrating the applicability of the method to degraded devices. Both current-based and voltage-based sampling strategies were implemented. For partially shaded modules, despite the increased estimation uncertainty, the variance reductions remained significant, spanning from 14.5% to 99.9%. In the case of fully irradiated modules, the optimization process led to variance reductions ranging from 88.0% to 99.9% across all parameters and strings. These results highlight the robustness and effectiveness of the proposed D-optimal sampling strategy in reducing parameter uncertainty under real-world operating conditions.

The proposed technique bridges the gap between the use of the perturb-and-observe algorithm and the full-span measurement of the I–V curve, by identifying the specific points along the I–V curve that carry the most significant information, making them optimal for measurement. In particular, this analysis highlights that the most influential regions of the I–V curve for PV module parameter estimation are the short-circuit condition and the range immediately following the elbow of the I–V curve. Such an approach can be particularly useful to provide guidance on which parts of the curve should be prioritized for accurate parameter estimation.

The rationale behind the use of current-based sampling throughout this work lies in its effectiveness under partial shading conditions. In such scenarios, sub-modules within the PV module experience different irradiance levels but are electrically connected in series. As a result, all sub-modules share the same current, which makes current sampling essential to preserve the physical consistency of the measurement. This approach enables the independent estimation of parameters, CRLB, and optimal sampling strategies for each sub-module, even when their conditions differ.

Conversely, in uniformly irradiated and healthy modules, where all sub-modules are exposed to the same conditions and expected to behave similarly, voltage-based sampling is a viable and often more practical alternative. This is particularly relevant when the measurement setup favours voltage control over current control, as is common in many laboratory and power plant environments.

In addition, the proposed method significantly enhances the accuracy of PV module parameter estimation, which is crucial for the operation and maintenance of PV plants. By supplying precise and reliable parameters, it allows operators to be immediately notified when faulty or degraded modules are detected, allowing rapid action to be taken. The suspect modules can then be subject to further testing using thermography or electroluminescence, ensuring these complementary techniques are used more efficiently and only when needed. This integrated approach not only provides significant support to plant diagnostics but also supports the long-term operational performance of PV systems, offering a robust framework for practical implementation.

Despite its advantages, the proposed methodology presents some limitations. It is worth noting that the optimization procedure for 50 points requires approximately 14 seconds of computation time on a standard personal computer. As such, the current implementation is more suitable for offline analysis and is not yet compatible with applications that require strict real-time constraints, such as high-speed Maximum Power Point (MPP) Tracking. In this context, the evaluation of the Fisher Information Matrix over multiple sampling points may also be computationally demanding for embedded platforms. To address this, future research may explore surrogate modelling techniques, such as proper orthogonal decomposition or Gaussian process regression, to accelerate the design step and enable real-time applicability.

Moreover, the method assumes a known parametric model structure and measurement noise distribution. While the formulation remains valid for any analytically characterized noise model, the current implementation relies upon the Gaussian IID case and does not account for heavy-tailed errors, sensor drift, or correlated noise. Robust estimation techniques and change detection mechanisms may be integrated in future versions to handle such deviations and support recalibration under ageing-related effects like soiling or micro-cracks.

The results of the analysis have been reported considering the five-parameter single-diode equivalent circuit model. While this choice ensures tractability and general applicability, extending the D-optimal design framework to support more sophisticated representations, such as two-diode or degradation-aware models, would further improve its relevance in diverse PV technologies. Such extensions could include model selection mechanisms based on information-theoretic criteria, allowing the identification of both optimal sampling patterns and the most suitable model structure.

REFERENCES

[1] S. Schubert, G. Malgaroli, and F. Spertino, "Experimental analysis of equivalent circuit's parameters for half-cell photovoltaic modules under natural sunlight," in *Proc. IEEE Int. Instrum. Meas. Technol. Conf. (I2MTC)*, May 2024, pp. 1–6.

[2] Y. Zhu and W. Xiao, "A comprehensive review of topologies for photovoltaic I–V curve tracer," *Sol. Energy*, vol. 196, pp. 346–357, Jan. 2020.

[3] H. Wu and Z. Shang, "Research on parameter extraction method of photovoltaic module based on improved hybrid algorithm," *Int. J. Photoenergy*, vol. 2020, pp. 1–12, Jan. 2020.

[4] S. R. Fahim, H. M. Hasanien, R. A. Turky, S. H. E. A. Aleem, and M. Ćalasan, "A comprehensive review of photovoltaic modules models and algorithms used in parameter extraction," *Energies*, vol. 15, no. 23, p. 8941, Nov. 2022.

[5] M. Q. Baig, H. A. Khan, and S. M. Ahsan, "Evaluation of solar module equivalent models under real operating conditions—A review," *J. Renew. Sustain. Energy*, vol. 12, no. 1, Jan. 2020, Art. no. 012701.

[6] M. Jobayer, M. A. H. Shaikat, M. Naimur Rashid, and M. R. Hasan, "A systematic review on predicting PV system parameters using machine learning," *Heliyon*, vol. 9, no. 6, Jun. 2023, Art. no. e16815.

[7] P. Changmai, S. Deka, S. Kumar, T. S. Babu, B. Aljafari, and B. Nastasi, "A critical review on the estimation techniques of the solar PV cell's unknown parameters," *Energies*, vol. 15, no. 19, p. 7212, Sep. 2022.

[8] Z. Gu, G. Xiong, and X. Fu, "Parameter extraction of solar photovoltaic cell and module models with metaheuristic algorithms: A review," *Sustainability*, vol. 15, no. 4, p. 3312, Feb. 2023.

[9] J. Xu, "Separable nonlinear least squares search of parameter values in photovoltaic models," *IEEE J. Photovolt.*, vol. 12, no. 1, pp. 372–380, Jan. 2022.

[10] A. Angulo, M. Huerta, and F. Mancilla-David, "A neural network-aided functional model of photovoltaic arrays for a wide range of atmospheric conditions," *IEEE Trans. Ind. Informat.*, vol. 20, no. 2, pp. 2487–2496, Feb. 2024.

[11] P. J. Gnetchejo, S. N. Essiane, A. Dadjé, P. Ele, D. E. M. Wapet, S. P. Ngoffe, and Z. Chen, "A self-adaptive algorithm with Newton Raphson method for parameters identification of photovoltaic modules and array," *Trans. Electr. Electron. Mater.*, vol. 22, no. 6, pp. 869–888, Dec. 2021.

[12] W. Xu, W. K. Wong, K. C. Tan, and J.-X. Xu, "Finding high-dimensional D-optimal designs for logistic models via differential evolution," *IEEE Access*, vol. 7, pp. 7133–7146, 2019.

[13] G. N. Tiwari and S. Dubey, *Fundamentals Photovoltaic Modules Their Applications*. London, U.K.: Royal Society of Chemistry, 2009.

[14] D. Wei, M. Wei, H. Cai, X. Zhang, and L. Chen, "Parameters extraction method of PV model based on key points of I–V curve," *Energy Convers. Manage.*, vol. 209, Apr. 2020, Art. no. 112656.

[15] C. S. Ruschel, F. P. Gasparin, and A. Krenzinger, "Experimental analysis of the single diode model parameters dependence on irradiance and temperature," *Sol. Energy*, vol. 217, pp. 134–144, Mar. 2021.

[16] V. Sovljanski and M. Paolone, "On the use of Cramér–Rao lower bound for least-variance circuit parameters identification of Li-ion cells," *J. Energy Storage*, vol. 94, Jul. 2024, Art. no. 112223.

[17] S. M. Kay, *Fundamentals of Statistical Signal Processing: Practical Algorithm Development*, vol. 3. London, U.K.: Pearson, 2013.

[18] K. W. Vugrin, L. P. Swiler, R. M. Roberts, N. J. Stucky-Mack, and S. P. Sullivan, "Confidence region estimation techniques for nonlinear regression in groundwater flow: Three case studies," *Water Resour. Res.*, vol. 43, no. 3, Mar. 2007, Art. no. W03423.

[19] C. R. Harris et al., "Array programming with NumPy," *Nature*, vol. 585, no. 7825, pp. 357–362, Sep. 2020.

[20] D. d. B. Mesquita, J. L. de S. Silva, H. S. Moreira, M. Kitayama, and M. G. Villalva, "A review and analysis of technologies applied in PV modules," in *Proc. IEEE PES Innov. Smart Grid Technol. Conf. Latin Amer. (ISGT Latin Amer.)*, Sep. 2019, pp. 1–6.

[21] P. Virtanen et al., "SciPy 1.0: Fundamental algorithms for scientific computing in Python," *Nature Methods*, vol. 17, no. 3, pp. 261–272, 2020.

[22] E. I. Batzelis, G. Anagnostou, C. Chakraborty, and B. C. Pal, "Computation of the Lambert W function in photovoltaic modeling," in *ELECTRIMACS 2019*. Berlin, Germany: Springer, 2020, pp. 583–595.

STEFANO SCHUBERT (Member, IEEE) received the B.Sc. degree in mechanical engineering and the M.Sc. degree in energy engineering from Politecnico di Torino, Turin, Italy, in 2019 and 2022, respectively, where he is currently pursuing the Ph.D. degree in electrical, electronics, and communications engineering. His research interests include the modeling of photovoltaic modules and the identification of their electrical parameters, with a focus on advanced characterization techniques and numerical simulation for performance prediction and optimization.

VLADIMIR SOVLJANSKI (Member, IEEE) received the B.Sc. degree (Hons.) in electrical and computer engineering from the Faculty of Technical Sciences, University of Novi Sad, Serbia, in 2018, and the M.Sc. degree in electrical and electronic engineering from the Swiss Federal Institute of Technology in Lausanne (EPFL), in 2021, where he is currently pursuing the Ph.D. degree with the Distributed Electrical Systems Laboratory. His research interests include battery modeling, characterization, and parameter identification.

FILIPPO SPERTINO (Senior Member, IEEE) received the M.Sc. degree and the Ph.D. degree in electrical engineering from Politecnico di Torino (PdT) University, Turin, Italy, in 1995 and 2000, respectively. He is currently a Full Professor in electric power systems and renewable energy systems with the College of Electrical Engineering and Energy Engineering of Energy Department, PdT. He is involved in the Italian branch of IEC regarding the grid connection of PV and wind power systems. He is the author/coauthor of more than 160 publications: 62 on Journals, two book chapters, and the remainder on proceedings of conferences. His research activities include design, simulation, experimental testing on photovoltaic/wind power systems, and instrument calibration.

GIANFRANCO CHICCO (Fellow, IEEE) received the Ph.D. degree in electrotechnics engineering. He is currently a Full Professor of electrical energy systems with Politecnico di Torino, Italy. His research interests include power system analysis, distribution system analysis and optimization, electrical load management, energy efficiency, and environmental impact of multi-energy systems, data analytics applied to power and energy systems, and power quality. He is the 2023–2024 Past-Chair of the IEEE R8 Italy Section. He was the Conference Chair of WESC 2006, IEEE PES ISGT Europe 2017, UPEC 2020, IEEE Eurocon 2023, and SEST 2024, and the Conference Co-Chair of IEEE SmartGridComm 2024. He is the Editor-in-Chief of *Sustainable Energy, Grids and Networks*.

MARIO PAOLONE (Fellow, IEEE) received the M.Sc. (Hons.) and Ph.D. degrees in electrical engineering from the University of Bologna, Italy, in 1998 and 2002, respectively. In 2005, he became an Assistant Professor of power systems with the University of Bologna, where he was with the Power Systems Laboratory, until 2011. Since 2011, he has been with the Swiss Federal Institute of Technology, Lausanne, Switzerland, where he is a Full Professor and the Chair of the Distributed Electrical Systems Laboratory. His research interests include power systems, with particular emphasis on real-time monitoring, operational aspects, protection, dynamics, and transients. He has made significant contributions in the field of PMU-based situational awareness for active distribution networks (ADNs) and in developing exact, convex, and computationally efficient methods for the optimal planning and operation of ADNs. He was the founding Editor-in-Chief of *Sustainable Energy, Grids and Networks* (Elsevier).